submitted to *Geophys. J. Int.*

The feasibility of thermal and compositional convection in Earth's inner core

Karen H. Lythgoe[1], John F. Rudge[1], Jerome A. Neufeld[1,2,3] & Arwen Deuss[1,4]

[1] *Bullard Laboratories, University of Cambridge, Madingley Road, Cambridge CB3 0EZ, UK*

[2] *BP Institute, Madingley Road, Cambridge, CB3 0EZ, UK*

[3] *Department of Applied Mathematics and Theoretical Physics, Wilberforce Road, Cambridge, CB3 0WA, UK*

[4] *Department of Earth Sciences, Universiteit Utrecht, Utrecht, Netherlands*

E-mail: khl43@cam.ac.uk

SUMMARY

Inner core convection, and the corresponding variations in grain size and alignment, has been proposed to explain the complex seismic structure of the inner core, including its anisotropy, lateral variations and the F-layer at the base of the outer core. We develop a parameterised convection model to investigate the possibility of convection in the inner core, focusing on the dominance of the plume mode of convection versus the translation mode. We investigate thermal and compositional convection separately so as to study the end-members of the system. In the thermal case the dominant mode of convection is strongly dependent on the viscosity of the inner core, the magnitude of which is poorly constrained. Furthermore recent estimates of a large core thermal conductivity result in stable thermal stratification, hindering convection. However, an unstable density stratification may arise due to the pressure dependant partition coefficient of certain light elements. We show that this unstable stratification leads to compositionally driven convection, and that inner core translation is likely to be the dominant convective mode due to the low compositional diffusivity. The style of convection resulting from a combination of both thermal and compositional effects is not easy to understand. For reasonable

parameter estimates, the stabilising thermal buoyancy is greater than the destabilising compositional buoyancy. However we anticipate complex double diffusive processes to occur given the very different thermal and compositional diffusivities.

Key words: Core, outer core and inner core; Numerical approximations and analysis; Composition of the core

1 INTRODUCTION

The inner core plays an important role in the dynamics of Earth's interior and understanding its dynamical state provides new and unique insights into the overall thermal and dynamical evolution of the Earth. As the Earth cools, the inner core grows by solidification of the surrounding fluid outer core (Jacobs 1953), releasing latent heat and light elements that provide a driving force for the geodynamo (Lister & Buffett 1995). The thermal and compositional structure of the inner core resulting from its gradual solidification may lead to internal convection (Jeanloz & Wenk 1988; Gubbins et al. 2013). Different modes of convection have been proposed to explain some of the seismically observed features of the inner core (Jeanloz & Wenk 1988; Buffett 2009; Alboussière et al. 2010; Monnereau et al. 2010).

Seismology, being the only method available to directly study the inner core, has revealed the existence of anisotropy (Morelli et al. 1986; Woodhouse et al. 1986) and significant degree 1 lateral variations (Tanaka & Hamaguchi 1997). In particular, the upper inner core is seismically isotropic and has a western hemisphere with an approximately 1 % slower isotropic P-wave velocity and greater attenuation than in the east (Niu & Wen 2001; Cao & Romanowicz 2004; Waszek et al. 2011). Cylindrical anisotropy – with compressional waves travelling fastest along Earth's rotation axis and slowest along the equatorial plane – appears from a depth of around 100 km below the inner core boundary (ICB) and is concentrated in a region in the western hemisphere (Tanaka & Hamaguchi 1997; Garcia & Souriau 2000; Creager 2000; Deuss et al. 2010; Irving & Deuss 2011; Lythgoe et al. 2014). The eastern region remains isotropic throughout the inner core (Lythgoe et al. 2014).

The dominant phase of iron at inner core conditions is most likely the hexagonal close packed (hcp) structure (Tateno et al. 2010; Stixrude 2012), which is strongly anisotropic (Stixrude & Cohen 1995; Martorell et al. 2013). It has been suggested that alignment of hcp crystals with Earth's rotation axis may explain the seismically observed cylindrical anisotropy (Stixrude & Cohen 1995), thus a mechanism is needed to align crystals.

The idea that thermal convection in the inner core aligns crystals through dislocation glide was first proposed by Jeanloz & Wenk (1988) and has been extensively studied since. Deguen & Cardin (2011) and Cottaar & Buffett (2012) used numerical thermochemical convection models to investigate the likelihood of high-Rayleigh number, plume style convection in a growing inner core. Both studies conclude that the inner core is more likely to thermally convect early in its history, but this result is dependent on several poorly constrained parameters, such as the heat flux at the core mantle boundary (CMB) and the core thermal conductivity. Buffett (2009) investigated the pattern of the flow as convection shuts down and showed that centrifugal acceleration may favour a final convective mode with a degree one pattern aligned with Earth's rotation axis. However the simulations of Deguen & Cardin (2011) suggest that there is insufficient stress associated with the last convective mode to produce an observable texture. Deguen et al. (2013) extended the model of Deguen & Cardin (2011) to include the effects of the phase change at the inner core boundary (ICB).

Recently, translation of the inner core – a convective mode whereby the whole inner core moves to the east due to enhanced solidification in the western hemisphere and melting in the east – was proposed to explain the seismic observations (Alboussière et al. 2010; Monnereau et al. 2010). The seismically observed hemispherical variations in isotropic velocity and attenuation in the upper inner core were explained by the grain growth associated with translation of inner core material (Monnereau et al. 2010; Geballe et al. 2013). Translation may also explain the anomalously low velocity layer at the base of the outer core, known as the F-layer (Souriau & Poupinet 1991; Song & Helmberger 1995; Yu et al. 2005; Zou et al. 2008), as a region of dense melt (Alboussière et al. 2010; Deguen et al. 2014). It is more difficult to explain lateral anisotropic variations since translation causes little or no deformation, but this may be explained by coexisting modes of translation and plume convection (Mizzon & Monnereau 2013).

However since thermally driven inner core convection was originally proposed, it has been suggested both experimentally and theoretically, that the thermal conductivity of the core is significantly higher than previously thought (Sha & Cohen 2011; de Koker et al. 2012; Pozzo et al. 2012; Gomi et al. 2013; Pozzo et al. 2014). Such high thermal conductivity values imply that thermal convection of the inner core is unlikely. However, the possibility remains that convection could be driven by compositional variations.

Compositional convection requires radial variations in the composition of the inner core. The core mainly consists of iron, but Birch (1952) showed that the outer core also contains a substantial amount of light elements. There is growing support for an outer core containing silicon (Georg et al. 2007; Fitoussi et al. 2009; Zieglera et al. 2010) and oxygen, (Badro et al. 2014) with the presence of elements such as sulphur, carbon or hydrogen remaining controversial (Hirose et al. 2013). Although light elements preferentially partition into the outer core (Alfè et al. 2002), a small amount of light elements must remain in the inner core to explain the observed density deficit (Jephcoat & Olson 1987). Gubbins et al. (2013) showed that, due to the temperature dependence of the partition coefficient of certain light elements, the inner core may become unstably stratified during its growth, thereby providing a possible mechanism for inner core convection. Labrosse (2014) also showed that compositional variations in the inner core can lead to unstable stratification, although his exact compositional profiles differ from those of Gubbins et al. (2013).

Previous studies of inner core thermal convection (Buffett 2009; Deguen & Cardin 2011; Cottaar & Buffett 2012; Deguen et al. 2013) used low values of thermal conductivity and assumed that compositional effects were stabilising. Given the uncertainty in physical properties, it remains unclear whether compositional or thermal convection in the inner core is possible and what the corresponding convective style might be.

In this paper we develop a parameterised model to investigate the possibility of thermal or compositional convection in the inner core. The model allows us to explore the dominance of the plume mode of convection with cold plumes sinking from the ICB and a passive return flow, versus the translation mode. Thermal and compositional convection are presented separately so as to study the end-members of the system. Section 2 outlines the inner core growth model used, which is based on global heat conservation. The parameterised thermal convection model is presented in section 3 and the method is adapted for compositional convection in section 4. We discuss the possible effects due to a combination of both thermal and compositional buoyancy in section 5.

2 GROWTH OF THE INNER CORE

As the core cools, the intersection of the adiabatic temperature with the liquidus temperature occurs at lower pressures, causing the inner core to grow (Figure 1). We model the growth of the inner core using the simple core thermal evolution model of Buffett et al. (1996), which is based on global heat conservation. Similar treatments are found in Roberts et al. (2003), Labrosse (2003) and Nimmo (2009). An energy budget for inner core growth equates the heat lost from the core at the core mantle boundary (CMB) to the total energy released in the outer and inner core,

$$\mathrm{Q_{CMB}} = \mathrm{Q_S} + \mathrm{Q_L} + \mathrm{Q_G}, \tag{1}$$

where $\mathrm{Q_{CMB}}$ is the total heat flow across the CMB, $\mathrm{Q_S}$ is the heat released by secular cooling of the core, $\mathrm{Q_L}$ represents latent heat released due to solidification of the inner core and $\mathrm{Q_G}$ is the change in gravitational energy associated with the exclusion of light elements at the ICB. Each energy term depends on the rate of inner core growth, $\mathrm{d}c/\mathrm{d}t$, where c is the radius of the inner core and t is time, as described in detail in Table 1. We assume for simplicity that $\mathrm{Q_{CMB}}$ is constant. It has been suggested that radioactive elements, particularly potassium, reside in the core (Murthy & Hall 1970; Roberts et al. 2003), but there is sufficient uncertainty regarding their availability that we neglect any energy contribution from internal heating. We also exclude the effect of a varying core composition on the liquidus, since the uncertainty in the value of CMB heat flux overwhelms this error.

The corresponding growth model for the inner core radius is

$$\frac{\mathrm{d}c}{\mathrm{d}t}\frac{1}{\mathcal{R}}\left(2c + \frac{3c^2}{b}\left(\mathcal{G} + \mathcal{L}\right)\right) = 1 \tag{2}$$

(Buffett et al. 1996), expressed in terms of three parameters, $\mathcal{R}$, $\mathcal{G}$, $\mathcal{L}$, and the outer core radius,

b. The parameter

$$\mathcal{R} = \frac{\mathrm{Q}_{\mathrm{CMB}}}{\frac{4\pi}{3}\rho C_p b \Theta_0} \tag{3}$$

is expressed as a function of Θ_0,

$$\Theta_0 = \frac{2\pi G \rho^2 b^2}{3}\left(\frac{\partial T_L}{\partial P} - \frac{\partial T_a}{\partial P}\right), \tag{4}$$

which represents the expected temperature drop on solidifying the entire core, where ρ is the average inner core density, C_p is the specific heat capacity, G is the gravitational constant and $\partial T_L/\partial P$ and $\partial T_a/\partial P$ are the liquidus and adiabatic gradients respectively, which we assume to be constant in the inner core. The dimensionless quantities

$$\mathcal{G} = \frac{2}{5}\frac{G b^2 \Delta\rho}{C_p \Theta_0}, \tag{5}$$

$$\mathcal{L} = \frac{L}{C_p \Theta_0}, \tag{6}$$

represent the effects of gravitational energy release due to compositional buoyancy and latent heat release respectively, where $\Delta\rho$ is the density jump due to compositional change across the ICB and L is latent heat. Using parameter values in Table 2, $\mathcal{L}$ = 0.73 , $\mathcal{G}$ = 0.22 and $\mathcal{R}$ = 6.47 $\times 10^{-5}$ $\mathrm{m^2 s^{-1}}$.

Values for $\mathrm{Q}_{\mathrm{CMB}}$ have been estimated from seismic observations of the D” discontinuity and the Clapeyron slope of the post-perovskite transition (Hernlund et al. 2005) or from the buoyancy flux of thermal plumes (Mittelstaedt & Tackley 2006), leading to a range from 7 to 15 TW. Solving (2) for the inner core radius as a function of time for this range of $\mathrm{Q}_{\mathrm{CMB}}$ estimates, results in a broad range of values for the age of the inner core, between 0.5 and 1.5 Byr (Figure 2). Recently, Gomi et al. (2013) have advocated for the CMB heat flux to be greater than 10 TW in order to power the dynamo with a high core thermal conductivity, resulting in an inner core that is less than 1 Byr old. This range of parameter estimates not only leads to variability in estimates of the growth history of the inner core, but also to uncertainty in estimates of its dynamic evolution.

3 THERMAL CONVECTION

3.1 Energy balance

For thermal convection to occur in the inner core, its internal temperature gradient must exceed the adiabatic gradient, i.e. it must be superadiabatic (Figure 1). During convection the internal temperature then evolves toward an adiabatic gradient. Changes over time in the internal temperature are governed by energy conservation – the total change in heat equals the heat gained from new material crystallising as the inner core grows, plus heat lost by conduction and thermal convection, written together as a single radial heat flux, q, such that

$$\frac{\mathrm{d}}{\mathrm{d}t}\int_V \rho C_p T\,\mathrm{d}V = \int_S \frac{\mathrm{d}c}{\mathrm{d}t}\rho C_p T_L\,\mathrm{d}S - \int_S q\,\mathrm{d}S, \tag{7}$$

where T is the internal inner core temperature, V and S are the volume and surface area of the inner core respectively, and T_L is the liquidus temperature at the ICB. We write (7) as

$$\frac{\mathrm{d}}{\mathrm{d}t}\left(\frac{4\pi}{3}\rho C_p c^3 \bar{T}(t)\right) = 4\pi c^2 \frac{\mathrm{d}c}{\mathrm{d}t}\rho C_p T_L - 4\pi c^2 \bar{q}, \tag{8}$$

where $\bar{T}$ and $\bar{q}$ are the volume averaged internal temperature and surface averaged radial heat flux respectively,

$$\bar{T}(t) = \frac{1}{\frac{4\pi}{3}c^3}\int_V T\,\mathrm{d}V, \quad \bar{q} = \frac{1}{4\pi c^2}\int_S q\,\mathrm{d}S. \tag{9}$$

Deviations from the adiabatic thermal profile drive the resulting dynamical response, and so we define a potential temperature,

$$\Theta(\mathbf{x}, t) = T(\mathbf{x}, t) - T_a(r, t), \tag{10}$$

as the difference between the temperature and the adiabatic temperature, T_a, such that the internal temperature is superadiabatic when Θ is positive. Note that at the ICB $\Theta = 0$. The mean potential temperature,

$$\bar{\Theta}(t) = \frac{1}{\frac{4\pi}{3}c^3}\int_V \Theta(\mathbf{x}, t)\,\mathrm{d}V = \bar{T}(t) - \bar{T}_a(t), \tag{11}$$

is the volume average of the potential temperature. In order to write the energy balance (8) in terms of the mean potential temperature, we first note that

$$\frac{\mathrm{d}}{\mathrm{d}t}\left(\frac{4\pi}{3}\rho C_p c^3 \bar{T}_a(t)\right) = \frac{\mathrm{d}}{\mathrm{d}t}\left(4\pi\rho C_p \int_0^{c(t)} r^2 T_a(r,t)\,\mathrm{d}r\right)$$
$$= 4\pi\rho C_p c^2 \frac{\mathrm{d}c}{\mathrm{d}t} T_a(c(t),t) + 4\pi\rho C_p \int_0^{c(t)} r^2 \frac{\partial T_a}{\partial t}\,\mathrm{d}r. \tag{12}$$

Using (11) and (12), the energy balance (8) is therefore

$$\frac{\mathrm{d}}{\mathrm{d}t}\left(\frac{4\pi}{3}\rho C_p c^3 \bar{\Theta}(t)\right) = -4\pi\rho C_p \int_0^{c(t)} r^2 \frac{\partial T_a}{\partial t}\,\mathrm{d}r - 4\pi c^2 \bar{q}. \tag{13}$$

Since the adiabat and liquidus intersect at the ICB, $T_a(c(t),t) = T_L(c(t))$, thus

$$\frac{\partial T_a}{\partial t} + \left.\frac{\partial T_a}{\partial r}\right|_{r=c} \frac{\mathrm{d}c}{\mathrm{d}t} = \left.\frac{\partial T_L}{\partial r}\right|_{r=c} \frac{\mathrm{d}c}{\mathrm{d}t}, \tag{14}$$

assuming that $\partial T_L/\partial t = 0$. We may therefore write the evolution of the adiabatic temperature as

$$\frac{\partial T_a}{\partial t} = \left(\left.\frac{\partial T_L}{\partial r}\right|_{r=c} - \left.\frac{\partial T_a}{\partial r}\right|_{r=c}\right)\frac{\mathrm{d}c}{\mathrm{d}t} = \left.\frac{\partial P}{\partial r}\right|_{r=c}\left(\frac{\partial T_L}{\partial P} - \frac{\partial T_a}{\partial P}\right)\frac{\mathrm{d}c}{\mathrm{d}t}. \tag{15}$$

Finally noting that

$$\frac{\partial P}{\partial r} = -\rho g(r) = -\rho g' r, \tag{16}$$

where $g' = \frac{4\pi}{3} G\rho$, the energy balance may be written as

$$\frac{\mathrm{d}}{\mathrm{d}t}\left(\frac{4\pi}{3}\rho C_p c^3 \bar{\Theta}(t)\right) = \frac{4\pi}{3}\rho^2 C_p g' c^4 \frac{\mathrm{d}c}{\mathrm{d}t}\left(\frac{\partial T_L}{\partial P} - \frac{\partial T_a}{\partial P}\right) - 4\pi c^2 \bar{q}, \tag{17}$$

assuming that $\partial T_a/\partial P$ and $\partial T_L/\partial P$ are uniform in the inner core. We use (17) to investigate the evolution of the mean potential temperature, $\bar{\Theta}$, as the inner core grows. The inner core growth rate, $\mathrm{d}c/\mathrm{d}t$, is determined from the growth model in section 2. The mean potential temperature evolves, as the inner core grows, according to the conductive or convective regime determining the radial heat flux, $\bar{q}$, as discussed in section 3.2.

3.2 Modes of heat transfer

The radial heat flux may be primarily conductive, plume convective, or given by the translational mode. Here we examine a simplified, and parametrised, model of the radial heat flux. Our parameterised model is similar to that of Cottaar & Buffett (2012), but includes the effect of inner core translation and we do not assume compositional effects to be stabilising.

Conduction down the adiabatic gradient provides a significant proportion of the radial heat flux. Therefore we parametrise the total heat flux into two parts: a heat flux due to conduction down the adiabatic gradient ($q_{adiabat}$), and a flux from the additional heat transfer that occurs due to the actual temperature gradient being sub- or super-adiabatic ($\tilde{q}$),

$$\bar{q} = q_{adiabat} + \tilde{q}. \tag{18}$$

In order to parametrise the additional heat loss due to the departure of the internal temperature from the adiabatic profile, we first derive asymptotic expressions for the heat flux assuming only one form of heat transport is occurring, deriving separate expressions for the additional heat transport by conduction (q_{diff}), heat transport by plume convection (q_{plume}), and heat transport by inner core translation (q_{trans}). We then approximate the total heat flux due to a combination of these mechanisms as the direct sum of the three asymptotic expressions,

$$\tilde{q} = q_{diff} + q_{plume} + q_{trans}. \tag{19}$$

The result is a single, simple parametrisation of the heat flux that provides a good approximation of the radial heat flux in parameter regimes in which there is a single dominant mode of heat transport. In the transition regions between different modes of heat transport the approximation above will be less accurate (see Appendix A for discussion on the accuracy of this approximation), but we will show that it provides a straightforward method for assessing the dynamical regime to sufficient accuracy, particularly given uncertainties in the material parameters.

In order to rigorously determine the dominant mode of convection, either the stability of each mode with respect to perturbations should be studied, or the full dynamical problem solved numerically. However our approach is to use a simple method, whereby we calculate (19) in order to ascertain the dominant mode of heat transport. This dominant, or largest contributing mode, is interpreted as the mode most likely to be observed in that region of parameter space. For example, we infer that translation is the dominant convective mode if q_{trans} is greater than both q_{plume} and q_{diff} (see Table 3). This is a relatively crude method to determine the likely mode of heat transport, but produces the correct order of magnitude behaviour, as is shown in section 3.3.2 by comparison of our parameterised model to the detailed analysis of Deguen et al. (2013) which solves the full set of governing equations. Therefore we verify posteriori that the inner core system is close to optimising heat transport and thus the convective mode that is most efficient is that which is most likely to be observed.

3.2.1 Conduction

The heat lost from conduction is given by the sum of the heat lost along the adiabat, $q_{adiabat}$, and the extra heat lost due to departure of the internal temperature from adiabatic equilibrium, q_{diff},

$$q_{cond} = q_{adiabat} + q_{diff}, \tag{20}$$

and may be evaluated from the temperature gradient at the ICB,

$$q_{cond} = -k \left.\frac{\partial T}{\partial r}\right|_{r=c} = -k \left.\frac{\partial P}{\partial r}\right|_{r=c} \left.\frac{\partial T}{\partial P}\right|_{ICB} = k\rho g' c \left.\frac{\partial T}{\partial P}\right|_{ICB}, \tag{21}$$

where we assume

$$P = P_0 - \frac{\rho g'}{2} r^2, \tag{22}$$

where P_0 is a reference pressure at the centre of the Earth.

For parameters relevant to the inner core the conductive temperature and adiabat are approximately linear functions of pressure (Buffett 2000), and hence

$$\Theta = T - T_a = \left(\frac{\partial T}{\partial P} - \frac{\partial T_a}{\partial P} \right) (P - P_{icb}). \tag{23}$$

By averaging (23) over the inner core and combining with (22), we find that the internal temperature gradient is given by

$$\frac{\partial T}{\partial P} = \frac{\partial T_a}{\partial P} + \frac{5\bar{\Theta}}{\rho g' c^2}. \tag{24}$$

Thus the conductive heat flux, q_{cond}, may be expressed in terms of the adiabat and the potential temperature

$$q_{cond} = k\rho g' c \frac{\partial T}{\partial P} = k\rho g' c \frac{\partial T_a}{\partial P} + 5k\frac{\bar{\Theta}}{c}, \tag{25}$$

where we define the heat lost by diffusion along the adiabat as

$$q_{adiabat} = k\rho g' c \frac{\partial T_a}{\partial P} \tag{26}$$

and the heat lost by diffusion due to the departure of the internal temperature from the adiabat as

$$q_{diff} = 5k\frac{\bar{\Theta}}{c}. \tag{27}$$

3.2.2 Plume convection

We next derive an expression for the heat flux from vigorous, plume convection, q_{plume} (see Deguen & Cardin (2011) and Cottaar & Buffett (2012)). The convective flux, q_{plume}, is parameterised following conventional scaling arguments that relate the Nusselt number,

$$\mathrm{Nu} = \frac{q_{plume}}{q_{diff}}, \tag{28}$$

which is a non-dimensional measure of the convective flux, to the Rayleigh number,

$$\mathrm{Ra} = \frac{\alpha g(c)\bar{\Theta}(c)c^3}{\kappa\nu}. \tag{29}$$

Here α is the coefficient of thermal expansion, $g(c)$ is the gravitational acceleration at the ICB, κ is the thermal diffusivity and ν is the kinematic viscosity. For $\mathrm{Ra} \gg \mathrm{Ra_c}$ we use the conventional scaling relationship $\mathrm{Nu} \sim \mathrm{Ra}^{\frac{1}{3}}$, where $\mathrm{Ra_c}$ is the critical Rayleigh number, above which convection occurs. This scaling relationship is based on the assumption that the timescale for convective overturn is small compared to any other timescales in the problem. In this high Ra regime the convective plume flux may be approximated as

$$q_{plume} = Bk\left(\frac{g'\alpha}{\nu\kappa}\right)^{1/3} c^{1/3}\bar{\Theta}^{4/3}, \tag{30}$$

where $q_{plume} = 0$ when $\bar{\Theta} < 0$ and $B = 0.48$ is a constant that is taken from the scaling laws derived from the numerical calculations of Deguen et al. (2013). This is similar to the value of $B = 0.49$ found from the numerical simulations of Cottaar & Buffett (2012).

3.2.3 Translation

Finally we derive the average radial heat flux due to inner core translation, q_{trans}. Translation, where the whole inner core moves at a uniform velocity, was first described by Alboussière et al.

(2010) and Monnereau et al. (2010). The inner core is displaced from its equilibrium position such that the ICB temperature does not correspond to the solidus and becomes unstable, resulting in melting on one side and crystallisation on the opposite side of the inner core. Topography is removed by phase change and restored by isostatic adjustment towards gravitational equilibrium.

We express the heat lost from translation using the analytical model of Alboussière et al. (2010), derived from a global force balance on the inner core. Thermal translation requires that the inner core has a global superadiabatic profile that is linear in the translation direction

$$\frac{\partial \Theta}{\partial x} = A, \tag{31}$$

where x is aligned with the axis of translation and A is a constant. At the ICB $\Theta = 0$ (ignoring a thin boundary layer on the melting side), so for $x < 0$

$$\Theta = A\left(r\cos\theta + \sqrt{c^2 - r^2\sin^2\theta}\right), \tag{32}$$

where θ is the angle between the $x-$axis and the point on the ICB. The mean potential temperature may now be written as

$$\bar{\Theta} = \frac{3A}{4\pi c^3}\int_{r=0}^{c}\int_{\theta=0}^{\pi}\int_{\phi=0}^{2\pi}\left(r\cos\theta + \sqrt{c^2 - r^2\sin^2\theta}\right)\, r^2\sin\theta\,\mathrm{d}r\,\mathrm{d}\theta\,\mathrm{d}\phi = \frac{3Ac}{4}, \tag{33}$$

hence,

$$\frac{\partial \Theta}{\partial x} = \frac{4\bar{\Theta}}{3c}. \tag{34}$$

The translation velocity governs the rate of crystallisation or melting and so the heat flux due to translation,

$$\mathbf{q_{trans}} = \rho C_p \Theta V \mathbf{i}, \tag{35}$$

is proportional to the translational velocity, V, where $\mathbf{q_{trans}}$ is the heat flux and $\mathbf{i}$ is a unit vector in the translation direction. The total heat loss from translation over the surface, S, of the inner core is therefore

$$Q_{trans} = \int_S \mathbf{q_{trans}}\cdot\mathbf{n}\,\mathrm{d}S = \int_V \nabla\cdot\mathbf{q_{trans}}\,\mathrm{d}V, \tag{36}$$

where $\mathbf{n}$ is the unit normal to the surface. Combining (34–36), the total heat loss over the surface of the inner core is therefore

$$Q_{trans} = \rho C_p V \int \frac{\partial \Theta}{\partial x} \mathrm{d}V = \frac{16\pi}{9} \rho C_p V c^2 \bar{\Theta}, \tag{37}$$

and the corresponding average radial heat flux is

$$q_{trans} = \frac{4}{9} \rho C_p V \bar{\Theta}. \tag{38}$$

We follow the derivation of Alboussière et al. (2010) to find an expression for the translation velocity. The displacement, δ, of the inner core from an equilibrium position of uniform density can be expressed as a function of the thermal gradient, $\partial\Theta/\partial x$,

$$\delta = \frac{\alpha \rho c^2}{5 \Delta \rho} \frac{\partial \Theta}{\partial x}. \tag{39}$$

This displacement causes a temperature difference, δT, between the liquidus and the adiabat along the ICB

$$\delta T = \rho_l g(c) \delta \cos\theta \left(\frac{\partial T_L}{\partial P} - \frac{\partial T_a}{\partial P} \right) \tag{40}$$

where ρ_l is the density of the outer core. The temperature change, δT, creates a thermal boundary layer in the outer core, with heat transfer proportional to $uc_p\delta T$, where $u \simeq 10^{-4}$ m/s (Bloxham & Jackson 1991) is the outer core fluid velocity near the ICB (assumed to be the same order of magnitude as the fluid velocity at the CMB). The heat transfer is accommodated by latent heat associated with the phase change along the boundary

$$LV \cos\theta = uC_p \delta T. \tag{41}$$

Combining (39 – 41), the translation velocity is given by

$$V = \frac{4\pi G}{15} \frac{uC_p \rho_l \rho^2}{L \Delta\rho} \alpha c^3 \frac{\partial \Theta}{\partial x} \left(\frac{\partial T_L}{\partial P} - \frac{\partial T_a}{\partial P} \right). \tag{42}$$

Using (4) and (34), we rewrite the velocity as

$$V = \frac{8}{15} \frac{uC_p \rho_l \alpha \Theta_0}{L \Delta\rho} \bar{\Theta} \left(\frac{c}{b} \right)^2, \tag{43}$$

and substituting (43) into (38), the average radial heat flux due to translation is written

$$q_{trans} = \frac{32}{135} \frac{u\rho C_p^2 \rho_l \alpha \Theta_0}{L \Delta\rho} \left(\frac{c}{b} \right)^2 \bar{\Theta}^2 \tag{44}$$

where $q_{trans} = 0$ when $\bar{\Theta} < 0$. This expression for the translation velocity is strictly only valid in the limit of a rigid inner core since it does not account for isostatic adjustment made via a secondary flow that acts to redistribute degree 1 density anomalies if the viscosity of the inner core is sufficiently low (Deguen et al. 2013). The effect of this on the transition from translation to plume convection is discussed in Appendix A.

3.3 Summary of governing equations

We have developed expressions for all contributions to the radial heat flux from the ICB and now summarise the governing equations. We re-arrange the global energy balance of (17)

$$\frac{\mathrm{d}}{\mathrm{d}t}\left(\frac{4\pi}{3}\rho C_p c^3 \bar{\Theta}(t)\right) = \frac{4\pi}{3}\rho C_p c^3 \mathcal{S} - 4\pi c^2 \tilde{q} \tag{45}$$

such that conduction down the adiabat, $q_{adiabat}$, is written as part of the source function, $\mathcal{S}$,

$$\mathcal{S} = \rho g' c \frac{\mathrm{d}c}{\mathrm{d}t}\left(\frac{\partial T_L}{\partial P} - \frac{\partial T_a}{\partial P}\right) - 3\kappa\rho g' \frac{\partial T_a}{\partial P}, \tag{46}$$

as defined by Deguen et al. (2013). The radial flux, $\tilde{q}$, defined in (19), only contains terms that depend on the mean potential temperature, $\bar{\Theta}$, with the diffusive, plume and translational fluxes given by (27), (30), and (44) respectively, with the limit $\tilde{q} = 0$ when $\bar{\Theta} = 0$. We solve the global energy balance of (45) for $\bar{\Theta}$ by making it dimensionless and combining with the growth model of (2) (Appendix B).

3.3.1 Quasi-steady state approximation

Lastly, by assuming that convection within the inner core is vigorous we can derive expressions that allow comparison of our results to previous work. With this assumption, the time scale of thermal relaxation due to convection (i.e. the time taken for a convective system to return to thermal equilibrium after any changes to the heat flux) is fast compared to the time scale of inner core growth, so the system is in a quasi-steady state. In this limit the dominant energy balance in (45) is between terms $\frac{4\pi}{3}\rho C_p c^3 \mathcal{S}$ and $4\pi c^2 \tilde{q}$, thus

$$\tilde{q} \sim \frac{\rho C_p c \mathcal{S}}{3}. \tag{47}$$

If plume convection is dominant, we use q_{plume} in (47) to write $\bar{\Theta}$ analytically

$$\bar{\Theta} \sim \left(\frac{1}{3B}\right)^{\frac{3}{4}} \left(\frac{\nu c^2 \mathcal{S}^3}{\kappa^2 g' \alpha}\right)^{\frac{1}{4}}. \tag{48}$$

This expression is compared to the scaling laws derived from the numerical models of Deguen et al. (2013) (Table 3, Deguen et al. (2013)) in order to determine the value of B that is used in (30). Alternatively if translation is dominant we can compare our results to that of Alboussière et al. (2010). Assuming translation is dominant we use q_{trans} in (47) to write

$$\bar{\Theta} \sim \left(\frac{135}{96}\frac{\mathcal{S}}{c}\frac{b^2 L \Delta\rho}{C_p u \rho_l \alpha \Theta_0}\right)^{\frac{1}{2}}. \tag{49}$$

Substituting this approximate expression for $\bar{\Theta}$ in the translation velocity (43), we get

$$V^2 \sim \frac{4\pi}{15}\frac{G u C_p \alpha \rho^2 \rho_l}{L\Delta\rho}\left(\frac{\partial T_L}{\partial P} - \frac{\partial T_a}{\partial P}\right)\mathcal{S}c^3 \tag{50}$$

which matches the expression for translation velocity given by Alboussière et al. (2010).

3.3.2 Comparison to full solution of governing equations

We use the quasi-steady state approximation above to find expressions for when each mode of heat transport is dominant in order to plot a regime diagram at a particular instance in time. Our regime diagram is compared to the regime diagram calculated by solving the full system of governing equations from Deguen et al. (2013), to allow us to understand the accuracy of our simple, parametrised model. In order to compare our models, we first non-dimensionalise each heat flux term, as detailed in Appendix C. Figure 3 shows our regime diagram, alongside that from Deguen et al. (2013), plotted for the Rayleigh number defined by Deguen et al. (2013), $\mathrm{Ra_d}$, as

$$\mathrm{Ra_d} = \frac{\alpha g' c^6 \mathcal{S}}{6\kappa^2 \nu}, \tag{51}$$

versus the dimensionless 'phase change' parameter, $\mathcal{P}$, defined by Deguen et al. (2013) as

$$\mathcal{P} = \frac{L\Delta\rho g' b^2 c}{2\rho\nu\Theta_0 u C_P}. \tag{52}$$

The dimensionless parameter $\mathcal{P}$ is the ratio of topographic production through solidification melting to viscous relaxation of induced topography. Hence $\mathcal{P}$ governs the type of convection that is dominant, with translation being dominant for low values of $\mathcal{P}$, while plume convection is dominant for high values of $\mathcal{P}$ and $\mathrm{Ra_d}$ (Figure 3).

We define one mode of heat transfer to be dominant when its flux has the largest contribution to the total heat flux (Table 3), defined by the solid line in Figure 3a. We also show when one mode of heat transfer is equal to the sum of the other two modes (dashed lines, Figure 3a) in order to highlight the transition region between modes. Within the transition regions our parametrisation results in an over estimate of the total heat flux, as explained in Appendix A by comparison to numerical experiments. Outside of the transition regions, a single mode of heat transport is dominant and so our asymptotic solutions capture the dynamics well in these regions of parameter space.

Our regime diagram approximately matches that obtained from the model of Deguen et al. (2013) (Figure 3b). We approximately match the critical values at which convection transitions between different modes in the asymptotic limits. For example we find the critical Rayleigh number to transition from the diffusion to plume mode to be 5.6 $\times 10^3$, while Deguen et al. (2013) obtain 1.5 $\times 10^3$, and our estimate of the transition from diffusion to translation is $\mathrm{Ra_d} \simeq 211\mathcal{P}$, while Deguen et al. (2013) obtain $\mathrm{Ra_d} \simeq 88\mathcal{P}$.

Interestingly, we also find a weak dependence of the transition from the plume mode to the translation mode on the Rayleigh number, with a scaling of $\mathrm{Ra_d} \simeq 7.87\mathcal{P}^2$ in the asymptotic limit. It is unclear if this dependence was also found in the study of Deguen et al. (2013) since they found a broad region where translation was important (up to $\mathcal{P} \sim 1000$). Additionally their study used Rayleigh numbers less than 10^7 only, therefore to confirm this dependence their analysis would need to be extended to higher values of $\mathrm{Ra_d}$. The different scalings may be due to different definitions of the transition from translation to plume dominant convection, between our parameterised model and the numerical model of Deguen et al. (2013). Deguen et al. (2013) define the transition from translation to plume modes to be the point at which small scale convective flow first emerges, which they interpret as being due to negative feedback of secondary flow on the translation mode. However, our definition is based on heat flux, and the transition from translation to plume modes occurs when the heat flux from plume convection is the largest contribution to the total flux, with the heat flux following the scaling in (30). This transition is discussed more fully in Appendix A.

3.4 Thermal results

We now use the theory derived above to study the different modes of thermal convection in the inner core. For comparison with previous studies, Figure 4 shows the thermal evolution of the inner core for a low thermal conductivity value of 36 W/m/K (Stacey & Davis 2008), calculated by solving the energy balance (45) for the mean potential temperature, $\bar{\Theta}$. For a $\mathrm{Q_{CMB}} = 11$ TW and a viscosity of $\mu = 10^{18}$ Pa s, $\bar{\Theta}$ is positive at all times, increasing as the size of the inner core grows, then decreasing as the rate of inner core growth slows (Figure 4a). A lower value of CMB heat flux (e.g. $\mathrm{Q_{CMB}} = 7$ TW, dotted line, Figure 4a) allows more time for heat to dissipate from the inner core, causing $\bar{\Theta} \to 0$ and any convection to stop at an earlier stage of inner core evolution, in agreement with Deguen & Cardin (2011) and Cottaar & Buffett (2012).

To investigate the dominant mode of convection, the average radial heat flux from the inner core is calculated for each convective mode, using equations (27), (30) and (44). The average radial heat flux follows a similar pattern to the mean potential temperature, first rising then decreasing. Translation is the dominant mode, except when the inner core is very young when diffusion dominates (Figure 4b). The corresponding translation velocity is on the order of 10^{-10} m s^{-1} (Figure 4c), around three times greater than the inner core growth rate, which is the minimum velocity at which seismic observations can be explained by translation (Monnereau et al. 2010). We also show the translation velocity calculated in the quasi-steady state approximation (dashed line, Figure 4c), which was used in the study by Alboussière et al. (2010). The quasi-steady state approximation causes an overestimation of the translation velocity compared to our model which does not require this approximation. We therefore use our solution in the remaining calculations.

We have used a representative CMB heat flux value of 11 TW, which fits within recent constraints (Lay et al. 2008; Gomi et al. 2013). Thermal convection does not occur for a $\mathrm{Q_{CMB}}$ less than approximately 6 TW, assuming a thermal conductivity of 36 W/m/K. For thermal convection to occur for higher thermal conductivity values, greater values of $\mathrm{Q_{CMB}}$ are required. For example a thermal conductivity of 200 W/m/K requires $\mathrm{Q_{CMB}} \geq 32$ TW for the inner core to be thermally unstable ($\bar{\Theta} > 0$) and convect.

An important parameter is the viscosity of the inner core which is poorly determined with published values ranging from 10^{11} Pa s (Van Orman 2004) to 10^{22} Pa s (Reaman et al. 2011). Thermal conductivity estimates have also changed significantly, from around 36 W/m/K (Stacey & Davis 2008) to over 200 W/m/K (de Koker et al. 2012; Pozzo et al. 2012). Therefore Figure 5a shows the dominant convective style for a range of inner core viscosity and thermal conductivity values, estimated by comparing the radial heat flux for each convective mode. The strength of plume convection (q_{plume}) versus translation (q_{trans}) is strongly dependent on the viscosity of the inner core (Figure 5b-d), with translation being dominant for viscosities above approximately 10^{18} Pa s, in agreement with Alboussière et al. (2010) and Deguen et al. (2013). Greater thermal conductivities cause convection to shut off at smaller inner core radii since the inner core becomes subadiabatic (Figure 5e), until thermal convection cannot occur for thermal conductivities greater than 68 W/m/K (Figure 5a). Given that the most recent estimates for core thermal conductivity are between approximately 150 and 240 W/m/K (Sha & Cohen 2011; de Koker et al. 2012; Gomi et al. 2013; Pozzo et al. 2012, 2014), thermal convection will not have occurred at any point in the inner core's lifetime. However, as we will show in section 4, compositional stratification may provide an alternative driving force for inner core convection.

4 COMPOSITIONAL CONVECTION

The seismically observed density jump at the ICB is too large to be explained solely by the density difference between the solid and liquid phase transition of iron and therefore requires enrichment of light elements in the fluid outer core relative to the solid inner core (Alfè et al. 2002). Jephcoat & Olson (1987) first showed that the inner core must also contain light elements due to the density deficit of the inner core with respect to the density of pure iron, with the main candidate light elements thought to be oxygen, sulphur and silicon (Hirose et al. 2013). Alfè et al. (2002) use ab initio calculations to examine the partitioning of sulphur, oxygen and silicon between solid and liquid at core conditions, estimating the light element concentration needed to match the seismically constrained ICB density jump. Their calculations show that oxygen partitions strongly from solid to liquid, while slightly more sulphur partitions into the liquid than the solid and silicon partitions equally between both phases.

In view of the fact that thermal convection in the inner core is unlikely for large estimates of the thermal conductivity, it is important to investigate the possibility of compositionally driven convection. It has previously been assumed that compositional variations in the inner core are stably stratified, hindering convection (Deguen & Cardin 2011; Cottaar & Buffett 2012). The stable stratification is the result of a constant partition coefficient over time, such that more light elements solidify in the inner core as the outer core concentration increases over time. However, Gubbins et al. (2013) recently showed that the light element concentration in the inner core may actually decrease as the inner core grows, because the partition coefficient is temperature dependent. In the case of sulphur and oxygen, this may result in a decreasing light element concentration with inner core radius, causing unstable stratification (Gubbins et al. 2013). Since silicon partitions equally between solid and liquid, its concentration does not change with time.

We first define the chemical potential, μ, of a phase in a multi-component system following Alfè et al. (2002),

$$\mu = \mu^0 + \lambda\chi + k_B T \ln\chi, \tag{53}$$

where μ^0 and λ are constants obtained from ab initio calculations, and represent a reference chemical potential and a linear correction from ab initio calculations respectively (Alfè et al. 2002), k_B is Boltzmann's constant, and χ is the molar ratio. Equilibrium at the solidification interface requires that the solid and liquid chemical potentials are equal, $\mu_s = \mu_l$, thus

$$\mu_l^0 + \lambda_l\chi_l^i(c) + k_B T_L(c)\ln\chi_l^i(c) = \mu_s^0 + \lambda_s\chi_s^i(c) + k_B T_L(c)\ln\chi_s^i(c), \tag{54}$$

where χ^i is the molar ratio at the solidification interface, denoted by superscript i and subscripts s and l represent solid and liquid respectively. The partition coefficient, P_{sl}, is the ratio of solid and liquid mole ratios at the ICB,

$$\mathrm{P}_{\mathrm{sl}} = \frac{\chi_s^i(c)}{\chi_l^i(c)} = \exp\left(\frac{\mu_l^0 + \lambda_l\chi_l^i(c) - \mu_s^0 - \lambda_s\chi_s^i(c)}{k_B T_L(c)}\right), \tag{55}$$

which is non-linear in χ_l^i and χ_s^i. The smaller the partition coefficient, the less light elements crystallise into the inner core. Due to the dependence of the partition coefficient on the liquidus, T_L, which is in turn dependent on pressure, the composition of material added to the inner core changes as the inner core grows. As in (23) we assume that the temperature gradient with pressure is constant and so express the liquidus at the ICB, $T_L(c)$, as a function of core radius by

$$T_L(c) = T_L(c_0) + \frac{1}{2}\frac{\mathrm{d}T_L}{\mathrm{d}P}\rho g'(c_0^2 - c^2), \tag{56}$$

where c_0 is the present day inner core radius. We neglect the effect of composition on the liquidus, since Labrosse (2014) showed this to be small.

We solve for the solid composition at the ICB, $\chi_s^i(c)$, by first assuming that the outer core is well mixed, such that the mean liquid composition, $\bar{\chi}_l$, equals the liquid composition at the solidification interface

$$\bar{\chi}_l(c) = \chi_l^i(c), \tag{57}$$

and so write the solid composition at the ICB explicitly in terms of the mean liquid concentration by re-arranging (55),

$$\chi_s^i(c) = \frac{k_B T_L(c)}{\lambda_s}\mathcal{W}\left[\frac{\bar{\chi}_l(c)\lambda_s}{k_B T_L(c)}\exp\left(\frac{\lambda_l\bar{\chi}_l(c) + \mu_l^0 - \mu_s^0}{k_B T_L(c)}\right)\right], \tag{58}$$

where $\mathcal{W}$ is the Lambert W function, defined by $z = \mathcal{W}(z)\exp^{\mathcal{W}(z)}$.

The average light element concentration in the inner and outer core, $\bar{\chi}_s(c)$ and $\bar{\chi}_l(c)$ respectively, are constrained by mass conservation, and fixed by the initial core concentration before inner core nucleation, χ_0. This implies

$$\frac{4\pi}{3}b^3\chi_0 = \frac{4\pi}{3}(b^3 - c^3)\bar{\chi}_l(c) + \frac{4\pi}{3}c^3\bar{\chi}_s(c), \tag{59}$$

where χ_0 is calculated from present day inner and outer core concentrations obtained from seismology (Table 4).

The validity of our assumption of a well-mixed outer core is somewhat uncertain, although if the seismically observed F-layer is a global, density-stratified layer, the analysis will hold assuming partitioning occurs over a layer of fluid (Gubbins et al. 2013).

4.1 Mass balance

We now construct a mass balance for light elements using an analogous approach to that used for heat in section 3.1. Equating the change in total moles of light element in the inner core with moles added at the ICB minus moles lost by diffusion and convection we obtain

$$\frac{\mathrm{d}}{\mathrm{d}t}\left(\frac{4\pi}{3}c^3\frac{\rho}{M}\bar{\chi}_s\right) = 4\pi c^2\frac{\mathrm{d}c}{\mathrm{d}t}\chi_s^i(t)\frac{\rho}{M} - 4\pi c^2 q_m, \tag{60}$$

where q_m is the molar flux and M is the average molar mass of the inner core.

Likewise, we now define a potential composition,

$$\phi(\mathbf{x}, t) = \chi_s(\mathbf{x}, t) - \chi_s^i(t), \tag{61}$$

as the difference between the light element composition in the inner core, χ_s, and the composition added at the ICB, χ_s^i, in a manner analogous to the potential temperature, such that $\phi > 0$ for convection to occur. The mean potential composition is defined as the volume average

$$\bar{\phi}(t) = \frac{1}{\frac{4\pi}{3}c^3}\int_V \phi(r, t)\,\mathrm{d}V = \bar{\chi}_s(t) - \chi_s^i(t). \tag{62}$$

Writing the mass conservation (60) in terms of the mean potential composition,

$$\frac{\mathrm{d}}{\mathrm{d}t}\left(\frac{4\pi}{3}c^3\frac{\rho}{M}\bar{\phi}\right) = \frac{4\pi}{3}c^3\frac{\rho}{M}\mathcal{S}_c - 4\pi c^2 q_m, \tag{63}$$

we obtain an equation which is analogous to the thermal energy balance in (45), using the source function from Deguen et al. (2013),

$$\mathcal{S}_c = -\frac{\mathrm{d}\chi_s^i}{\mathrm{d}t}, \tag{64}$$

which represents the change in composition of material added to the inner core as it grows.

Since the source term, (64), depends on the concentration in the outer core, we solve for the composition at the ICB, χ_s^i, and the potential composition, ϕ, simultaneously. This is done by making the mass conservation equation (63) dimensionless, and applying the non-dimensional growth model (Appendix D1). The dimensionless equation (D.1) is then solved together with (58), (59) and (62) as a system of differential algebraic equations (Appendix D2). A comparable treatment is performed by Labrosse (2014). Gubbins et al. (2013) simplify the problem by assuming that changes in the internal composition, $\bar{\chi}_s$, are small, allowing variations in the liquid concentration, $\bar{\chi}_l$, hence variations in the concentration added to the inner core, χ_s^i, to be calculated analytically (using (59) and (58) respectively). Before solving for χ_s^i and $\bar{\phi}$ we derive expressions for the radial molar flux, q_m, from the inner core as detailed below.

4.2 Modes of molar flux

We again approximate the radial flux to be the sum of contributions from compositional diffusion (q_{diff}), plume convection (q_{plume}) and translation (q_{trans}),

$$q_m = q_{diff} + q_{plume} + q_{trans}, \tag{65}$$

where q_m corresponds to molar flux. We find expressions for each molar flux term independently as a function of mean potential compositional, in a directly analogous manner to the thermal case discussed in section 3.2.

4.2.1 Diffusion

The diffusive radial flux is now parameterised using Fick's law for compositional diffusion, so that the compositional diffusive flux is

$$q_{diff} = -D \left.\frac{\partial \Phi}{\partial r}\right|_{r=c} = \frac{5D\Phi}{c}, \tag{66}$$

in analogy to (27), where D is the solid diffusivity and Φ is the average potential molar concentration

$$\Phi = \frac{\bar{\phi}\rho}{M}. \tag{67}$$

4.2.2 Plume convection

For the plume mode of convection a compositional Rayleigh number,

$$\mathrm{Ra}_{\mathrm{comp}} = \frac{\alpha_c g(c)\bar{\phi}(c)c^3}{D\nu}, \tag{68}$$

may be defined, where α_c is the compositional expansion coefficient. We assume the same high Ra scaling, $\mathrm{Nu}_{\mathrm{comp}} \sim \mathrm{Ra}_{\mathrm{comp}}{}^{\frac{1}{3}}$, and so express the convective flux from plume convection as

$$q_{plume} = BD\frac{\rho}{M}\left(\frac{g'\alpha_c}{\nu D}\right)^{1/3} c^{1/3}\bar{\phi}^{4/3}, \tag{69}$$

where we use $B = 0.48$ as before.

4.2.3 Translation

The analysis for the translation model based on potential temperature can be adapted for compositional effects (Deguen et al. 2013). In this instance density variations in the inner core arise from differences in the composition of the melting and crystallising sides of the inner core, causing a displacement in its centre of mass. Following the analysis for potential temperature in section 3.2.3, the molar flux from translation is

$$q_{trans} = \frac{4}{9}\frac{\rho}{M}V\bar{\phi}. \tag{70}$$

The rate of translation remains limited by the ability of the outer core to remove heat at the ICB and so the translation velocity is expressed

$$V = \frac{8}{15}\frac{uC_p\rho_l\alpha_c\Theta_0}{L\Delta\rho}\bar{\phi}\left(\frac{c^2}{b^2}\right). \tag{71}$$

4.3 Compositional results

We now use the theory above to study the different modes of compositional convection. We show results for sulphur and oxygen separately due to the uncertainty in core composition and since they may be considered as end members of a more complex Fe-O-S-Si system. We use present day core concentrations calculated for the ICB density jump obtained from the radially symmetric PREM model (Dziewonski & Anderson 1981). Calculations have also been performed for the model of Masters & Gubbins (2003), however we show only PREM values since we are interested in compositional variations over time and the PREM density jump is consistent with other Earth models (Kennett & Engdahl 1991; Kennett et al. 1995).

Figures 6 and 7 show the evolution and convective influence of sulphur and oxygen in the core respectively. The concentration of sulphur in the outer core increases as the inner core grows since the partition coefficient is less than 1 (Figure 6a). However the increasing liquid concentration trades off with the decrease in the partition coefficient as the ICB moves to lower pressures, causing the concentration of sulphur added at the ICB to decrease initially. The sulphur concentration begins to increase when the inner core has a radius of around 550 km (Figure 6b). The initial decrease of χ_s^i creates a positive potential composition (Figure 6c), which then decreases until it becomes negative at a radius of around 650 km. If there is no inner core convection ($q_{plume} = q_{trans} = 0$) the potential composition is slightly greater and becomes negative at a later time (dashed line, Figure 6c). Figure 6d shows that while the potential composition is positive, the inner core is convecting, with translation being the dominant mode with a translation velocity on the order of 10^{-11} m/s (Figure 6e).

The oxygen concentration also increases in the outer core as the inner core grows (Figure 7a). However unlike sulphur, the oxygen concentration added at the ICB continuously decreases (Figure 7b), resulting in a positive potential composition and an inner core that is still convecting today (Figures 7c, 7d). The dominant convective mode is translation, with a translation velocity on the order of 10^{-10} m/s (Figure 7e), which is similar to the rate of thermally driven translation.

Gubbins et al. (2013) and Labrosse (2014) also solved for the inner core interface composition, but their studies found differing solutions for a seemingly unresolved reason (Labrosse 2014). We match the results of Labrosse (2014), however find we can also match the results of Gubbins et al. (2013) by changing the treatment of the chemical potential at the solidification interface (dotted line, Figures 6b and 7b). Gubbins et al. (2013) assume present day compositions when calculating the partition coefficient (see (55)), while Labrosse (2014) update the interface composition as the system evolves, which is the correct treatment. In the case of oxygen, Gubbins et al. (2013) also neglected the linear ab initio corrections.

The solid diffusivity of sulphur and oxygen at core conditions is uncertain, with values likely to be less than that of the liquid (around 10^{-9} m^{2}s^{-1} Gubbins et al. (2013)). Figures 8 and 9 show the model space for a range of mass diffusivity and inner core viscosity values, for sulphur and oxygen respectively. It is clear that translation is the dominant mode, except if the inner core viscosity is low and the diffusivity is high when plume convection dominates while the inner core is young.

5 COMBINED THERMAL AND COMPOSITIONAL EFFECTS

The convection resulting from solely thermal or compositional effects is now well understood, with our analysis showing that translation is likely to be the dominant convective style, particularly for compositional convection. However it is not trivial to understand the style of convection arising from a combination of both thermal and compositional diffusion.

Labrosse (2014) argues that the total buoyancy can be approximated from the sum of all thermal and compositional effects,

$$\frac{\delta\rho}{\rho_{ICB}} = \alpha\bar{\Theta} + \alpha_c^o\bar{\phi}^o + \alpha_c^s\bar{\phi}^s, \tag{72}$$

where superscripts s and o correspond to sulphur and oxygen respectively and $\delta\rho/\rho_{ICB}$ is the density anomaly relative to an adiabatic reference state, such that the system is unstable while $\delta\rho/\rho_{ICB} > 0$. We calculate this density anomaly for several thermal conductivity values and a combination of thermal and compositional effects using results from our end-member simulations, as shown in Figure 10. The density anomaly is primarily controlled by the thermal instability and is always negative for a thermal conductivity of 75 W/m/K or greater, independent of the inclusion of compositional effects.

However, we note that even if the net density gradient is stabilising, convection may occur through double diffusive convection (convection driven by two components with different rates of diffusion, see Huppert & Turner (1981)) since the rates of thermal and compositional diffusion differ by approximately 10^6. For instance, if the thermal conductivity is very large, any temperature anomalies will rapidly dissipate leading to a uniform thermal field, leaving only the possibility of compositionally driven convection remaining. Therefore it is possible that compositional convection may play the dominant role, particularly given the uncertainty in thermal conductivity estimates for the inner core.

6 DISCUSSION

We have shown that thermal convection occurs in the inner core for a thermal conductivity less than approximately 68 W/m/K (assuming parameters from Table 2). However this value depends on the assumed value of CMB heat flux and is also sensitive to uncertainties in outer core properties, significantly the difference between the Clapeyron and adiabatic gradients. For thermal convection to occur for higher thermal conductivity values requires the CMB heat flux to be greater than

30 TW, which is significantly higher than recent estimates. In the case of thermal convection, translation is the dominant mode for an inner core with a high viscosity, approximately greater than 10^{18} Pa s (Figure 5).

A wide range of values for the viscosity of the inner core have been estimated, ranging from 10^{11} to 10^{22} Pa s (Van Orman 2004; Dumberry & Bloxham 2002; Reaman et al. 2011). The most recent estimates of 10^{17} Pa s and 10^{15} – 10^{18} Pa s come from length of day variations (Davies et al. 2014) and from mineral physics experiments (Gleason & Mao 2013) respectively. The uncertainty in the viscosity of the inner core causes uncertainty in the type of convection occurring in the inner core, particularly for thermal convection.

We have also shown that compositional stratification can provide another driving force for convection in the inner core. Oxygen always generates an unstable density profile (Figure 6), while sulphur generates an unstable profile until the inner core reaches a radius of approximately 650 km, when it becomes stabilising (Figure 7). For both oxygen and sulphur, translation is the likely mode of convection, although there is a weak dependence on viscosity and diffusivity (Figures 8 and 9).

The value of the solid diffusivity of sulphur and oxygen at core conditions is uncertain, although it is likely to be less than the liquid diffusivity. This low diffusivity favours translation of the inner core and so uncertainty in the inner core viscosity is less important for compositional convection (Figures 8 and 9) than for thermal convection.

The translation velocity, for translation driven by variations in temperature and oxygen composition, is sufficient to explain the seismic structure of the upper inner core according to the model of Monnereau et al. (2010). However, since the rate of translation is primarily controlled by the ability of the outer core to extract or provide heat at the ICB, a change in the outer core fluid velocity also changes the translation velocity by the same amount. Thus if the outer core fluid velocity at the ICB is one order of magnitude less than that at the CMB (the estimate that is currently used), then the rate of translation will be too slow to explain the lateral variations in the upper inner core.

The composition of the core is still controversial and we consider only the model of Alfè et al. (2002), based on the average Earth model of PREM (Dziewonski & Anderson 1981) in this work, since all relevant parameters are given. This choice was sufficient for our study since our primary aim was to demonstrate that compositional variations in the inner core over time may drive inner core convection. However better knowledge of the composition of the core is needed before definitive conclusions regarding inner core convection can be drawn.

There is also large uncertainty in the remaining core parameters, significantly in the CMB heat flux, which controls the rate at which the core cools and the inner core grows. In order to narrow the parameter space, better constraints on these important parameters are needed.

Lastly, even if translation is occurring in the inner core, an explanation for lateral anisotropy variations still remains elusive. The most likely explanation for cylindrical anisotropy is the bulk alignment of intrinsically anisotropic crystals, thus a mechanism is needed to generate crystal alignment in the western 'hemisphere', with random bulk crystal alignment in the remaining inner core. Since very little deformation accompanies translation of the inner core, it is unlikely that translation will generate crystal alignment. It is possible that translation could be accompanied by another mechanism that orientates crystals, such as preferred equatorial solidification (Yoshida et al. 1996), or deformation due to Maxwell stresses (Karato 1999; Buffett & Wenk 2001). However any accompanying deformation mechanisms would need to work in an inner core with a high viscosity, since this is required for inner core translation.

7 CONCLUSIONS

The parameterised convection model we present approximates the total heat or compositional flux from the inner core as the sum of the heat or composition lost through conduction, plume convection and translation. We use our parameterised model to study the likelihood of either thermal or compositional convection in the inner core and assume the dominant convective mode to be the greatest contribution to the total flux. We find that thermal convection is unlikely to occur for the most recent estimates of core thermal conductivity unless the CMB heat flux is unreasonably large. However a translating convective mode may be driven in the inner core by compositional variations. By simply linearly combining the thermal and compositional buoyancy it appears that the inner core is stably stratified, unless the thermal conductivity is small. We suggest that future work might profitably focus on the possible double diffusive effects, that are often complex and unexpected (Huppert & Turner 1981), arising from a combination of both thermal and compositional buoyancy, potentially still making inner core convection feasible.

8 ACKNOWLEDGEMENTS

We would like to thank Chris Davies for help with comparison to his results, plus Deputy Editor Stéphane Labrosse, Renaud Deguen and an anonymous reviewer for constructive comments that improved the manuscript. KHL and AD are funded by the European Research Council under the European Community's Seventh Framework Programme (FP7/2007-2013)/ERC grant agreement number 204995. JAN is partially funded by a Royal Society University Research Fellowship.

REFERENCES

Alboussière, T., Deguen, R., & Melzani, M., 2010. Melting-induced stratification above the Earth's inner core due to convective translation, *Nature*, **2466**, 744 – 747.

Alfè, D., Price, G. D., & Gillan, M. J., 2002. Ab intio chemical potentials of solid and liquid alloys and the chemistry of the Earth's core, *J. Chem. Phys.*, **116**, 7127 – 7136.

Badro, J., Cote, A. S., & Brodholt, J. P., 2014. A seismologically consistent compositional model of Earth's core, *Proc. Natl. Acad. Sci. USA*.

Birch, F., 1952. Elasticity and constitution of the Earth's interior, *J. Geophys. Res.*, **2**.

Bloxham, J. & Jackson, A., 1991. Fluid flow near the surface of the Earth's outer core, *Rev. Geophys.*, **29**, 97 – 120.

Buffett, B. & Wenk, H. R., 2001. Texturing of the Earth's inner core by Maxwell stresses, *Nature*, **413**, 60 – 63.

Buffett, B. A., 2000. Dynamics of the Earth's core, *Geophys. Monograph AGU*, **117**, 37 – 62.

Buffett, B. A., 2009. Onset and orientation of convection in Earth's inner core, *Geophys. J. Int.*, **179**, 711 – 719.

Buffett, B. A., Huppert, H. E., & Lister, J. R., 1996. On the thermal evolution of the Earth's core, *J. Geophys. Res.*, **101**, 7989 – 8006.

Cao, A. & Romanowicz, B., 2004. Hemispherical transition of seismic attenuation at the top of the Earth's inner core, *Earth Planet. Sci. Lett.*, **228**, 243 – 253.

Cottaar, S. & Buffett, B., 2012. Convection in the Earth's inner core., *Phys. Earth Planet. Inter.*, **198**, 67 – 78.

Creager, K. C., 2000. Inner core anisotropy and rotation, *Geophys. Monograph AGU*, **117**, 89 – 114.

Davies, C. J., Stegman, D. R., & Dumberry, M., 2014. The strength of gravitational core-mantle coupling, *Geophys. J. Int.*.

de Koker, N., Steinle-Neumann, G., & Vlcek, V., 2012. Electrical resistivity and thermal conductivity of liquid Fe alloys at high P and T, and heat flux in Earth's core, *Proc. Natl. Acad. Sci. USA*, **109**, 4070 – 4073.

Deguen, R. & Cardin, P., 2011. Thermochemical convection in Earth's inner core, *J. Geophys. Res.*, **187**, 1101 – 1118.

Deguen, R., Alboussière, T., & Cardin, P., 2013. Thermal convection in Earth's inner core with phase change at its boundary, *Geophys. J. Int.*, **194**, 1310 – 1334.

Deguen, R., Olson, P., & Reynolds, E., 2014. F-layer formation in the outer core with asymmetric inner core growth, *Compteus Rendus Geoscience*, **346**, 101 – 109.

Deuss, A., Irving, J. C. E., & Woodhouse, J. H., 2010. Regional variation of inner core anisotropy from seismic normal mode observations, *Science*, **328**, 1018 – 1020.

Dumberry, M. & Bloxham, J., 2002. Inner core tilt and polar motion., *Geophys. J. Int.*, **151**, 377 – 392.

Dziewonski, A. M. & Anderson, D. L., 1981. Preliminary reference Earth model, *Phys. Earth Planet. Inter.*, **25**, 297 – 356.

Fitoussi, C., Bourdon, B., Kleine, T., Oberli, F., & Reynolds, B. C., 2009. Si isotope systematics of meteorites and terrestrial peridotites: implications for Mg/Si fractionation in the solar nebula and for Si in the Earth's core, *Earth Planet. Sci. Lett.*, **287**, 77 – 85.

Garcia, R. & Souriau, A., 2000. Inner core anisotropy and heterogeneity level, *Geophys. Res. Lett.*, **27**, 3121 – 3124.

Geballe, Z. M., Lasbleis, M., Cormier, V. F., & Day, E. A., 2013. Sharp hemisphere boundaries in a translating inner core, *Geophys. Res. Lett.*, **40**, 1719 – 1723.

Georg, R. B., Halliday, A. N., Schauble, E. A., & Reynolds, B. C., 2007. Silicon in the Earth's core, *Nature*, **447**, 1102 – 1106.

Gleason, A. E. & Mao, W. L., 2013. Strength of iron at core pressure and evidence for a weak Earth's inner core, *Nature Geosci.*, **6**, 571 – 574.

Gomi, H., Ohta, K., Hirose, K., Labrosse, S., Caracas, R., Verstraete, M. J., & Hernlund, J. W., 2013. The high conductivity of iron and thermal evolution of the Earth's core, *Phys. Earth Planet. Inter.*, **224**, 88 – 103.

Gubbins, D., Alfè, D., & Davies, C. J., 2013. Compositional instability of Earth's solid inner core, *Geophys. Res. Lett.*, **40**, 1084 – 1088.

Hernlund, J. W., Thomas, C., & Tackley, P. J., 2005. A doubling of the post-perovskite phase boundary and structure of the Earth's lowermost mantle, *Nature*, **434**, 882 – 886.

Hirose, K., Labrosse, S., & Hernlund, J., 2013. Composition and state of the core, *Ann. Rev. Earth Planet Sci.*, **41**, 657 – 691.

Huppert, H. E. & Turner, J. S., 1981. Double-diffusive convection, *J. Fluid.Mech.*, **106**, 299 – 329.

Irving, J. C. E. & Deuss, A., 2011. Hemispherical structure in inner core velocity anisotropy, *J. Geophys. Res.*, **116**, 1 – 17.

Jacobs, J. A., 1953. The Earth's inner core, *Nature*, **172**, 297 – 298.

Jeanloz, R. & Wenk, H. R., 1988. Convection and anisotropy of the inner core, *Geophys. Res. Lett.*, **15**, 72 – 75.

Jephcoat, A. & Olson, P., 1987. Is the inner core of the Earth pure iron?, *Nature*, **325**, 332 – 335.

Karato, S., 1999. Seismic anisotropy of the Earth's inner core resulting from flow induced by Maxwell stresses, *Nature*, **402**, 871 – 873.

Kennett, B. L. N. & Engdahl, E. R., 1991. Travel times for global earthquake location and phase identification, *Geophys. J. Int.*, **105**, 429 – 465.

Kennett, B. L. N., Engdahl, E. R., & Buland, R., 1995. Constraints on seismic velocities in the Earth from traveltimes, *Geophys. J. Int.*, **122**, 108 – 124.

Labrosse, S., 2003. Thermal and magnetic evolution of the Earth's core, *Earth Planet. Sci. Lett.*, **140**, 127 – 143.

Labrosse, S., 2014. Thermal and compositional stratification of Earth's inner core, *Compteus Rendus Geoscience*, **346**, 119 – 129.

Lay, T., Hernlund, J., & Buffett, B., 2008. Core-mantle boundary heat flow, *Nature Geosci.*, **1**, 25 – 32.

Lister, J. A. & Buffett, B. A., 1995. The strength and efficiency of thermal and compositional convection in the geodynamo, *Phys. Earth Planet. Inter.*, **91**, 17 – 30.

Lythgoe, K. H., Deuss, A., Rudge, J. F., & Neufeld, J. A., 2014. Earth's inner core: Innermost inner core or hemispherical variations?, *Earth Planet. Sci. Lett.*, **385**, 181 – 189.

Martorell, B., Brodholt, J., Wood, I. G., & Vocadlo, L., 2013. The effect of nickel on properties of iron at the conditions of Earth's inner core: Ab initio calculations of seismic wave velocities of Fe-Ni alloys, *Earth Planet. Sci. Lett.*, **365**, 143 – 151.

Masters, G. & Gubbins, D., 2003. On the resolution of density within the Earth, *Phys. Earth Planet. Inter.*, **140**, 159 – 167.

McKenzie, D. P., Roberts, J. M., & Weiss, N. O., 1974. Convection in the Earth's mantle: towards a numerical simulation, *J. Fluid.Mech.*, **62**, 465 – 538.

Mittelstaedt, E. & Tackley, P. J., 2006. Plume heat flow is much lower than CMB heat flow, *Earth Planet. Sci. Lett.*, **241**, 202 – 210.

Mizzon, H. & Monnereau, M., 2013. Implication of the lopsided growth for the viscosity of Earth's inner core, *Earth Planet. Sci. Lett.*, **361**, 391 – 401.

Monnereau, M., Calvet, M., Margerin, L., & Souriau, A., 2010. Lopsided growth of the Earth's inner core, *Science*, **328**, 1014 – 1017.

Morelli, A., Dziewonski, A. M., & Woodhouse, J. H., 1986. Anisotropy of the inner core inferred from PKIKP travel times, *Geophys. Res. Lett.*, **13**, 1545 – 1548.

Murthy, V. R. & Hall, H. T., 1970. The chemical composition of the Earth's core: possibility of sulphur in the core, *Phys. Earth Planet. Inter.*, **2**, 276 – 282.

Nimmo, F., 2009. Energetics of the Core, *Treatise on Geophysics*, **8**, 31 – 65.

Niu, F. & Wen, L., 2001. Hemispherical variations in seismic velocity at the top of Earth's inner core, *Nature*, **410**, 1081 – 1084.

Pozzo, M., Davies, C., Gubbins, D., & Alfè, D., 2012. Thermal and electrical conductivity of iron at Earth's core conditions, *Nature*, **485**, 355 – 358.

Pozzo, M., Davies, C., Gubbins, D., & Alfè, D., 2014. Thermal and electrical conductivity of solid iron and iron-silicon mixtures at Earth's core conditions, *Earth Planet. Sci. Lett.*, **393**, 159 – 164.

Reaman, D. M., Daehn, G. S., & Panero, W. S., 2011. Predictive mechanism for anisotropy development in Earth's inner core, *Earth Planet. Sci. Lett.*, **312**, 437 – 442.

Roberts, P. H., Jones, C. A., & Calderwood, A. R., 2003. *Energy fluxes and ohmic dissipation in the Earth's core*, In *Earth's core and the lower mantle* ed. Jones, C. A., Soward, A. M. and Zhang, K.

Sha, W. & Cohen, R. E., 2011. First principal studies of electrical resistivity of iron under pressure, *J. Phys.Condens.Matter*, **23**, 1 – 5.

Song, X. D. & Helmberger, D. V., 1995. A P-wave velocity model of Earth's core, *J. Geophys. Res.*, **100**, 9817 – 9830.

Souriau, A. & Poupinet, G., 1991. The velocity profile at the base of the liquid core from PKP(bc+cdiff) data: an argument in favour of radial inhomegeneity, *Geophys. Res. Lett.*, **18**, 2023 – 2026.

Stacey, F. D. & Davis, P. M., 2008. *Physics of the Earth*, Cambridge University Press, 4th edn.

Stixrude, L., 2012. Structure of iron to 1 Gbar and 40000 K, *Phys. Rev. Lett.*, **108**, 055505.

Stixrude, L. & Cohen, R. E., 1995. High-pressure elasticity of iron and anisotropy of the Earth's inner core, *Science*, **267**, 1972 – 1975.

Tanaka, S. & Hamaguchi, H., 1997. Degree one heterogeneity and hemispherical variation of anisotropy in the inner core from PKP(BC)-PKP(DF) times, *J. Geophys. Res.*, **102**, 2925 – 2938.

Tateno, S., Hirose, K., Ohishi, Y., & Tatsumi, Y., 2010. The structure of iron in the Earth's inner core, *Science*, **330**, 359 – 361.

Van Orman, J. A., 2004. On the viscosity and creep mechanism of Earth's inner core, *Geophys. Res. Lett.*, **31**, 1 – 4.

Vocadlo, L., 2007. Ab initio calculations of the elasticity of iron and iron alloys at inner core conditions: evidence for a partially molten inner core?, *Earth Planet. Sci. Lett.*, **254**, 227 – 232.

Vocadlo, L., Alfè, D., Gillan, M., & Price, G., 2003. The properties of iron under core conditions from first principle calculations., *Phys. Earth Planet. Inter.*, **140**, 101 – 125.

Waszek, L., Irving, J., & Deuss, A., 2011. Reconciling the hemispherical structure of the Earth's inner core with its super-rotation, *Nature Geosci.*, **4**, 264 – 267.

Woodhouse, J. H., Giardini, D., & Li, X. D., 1986. Evidence for inner core anisotropy from free oscillations, *Geophys. Res. Lett.*, **13**, 1549 – 1552.

Yoshida, S., Sumita, I., & Kumazawa, M., 1996. Growth model of the inner core coupled with outer core dynamics and the resulting elastic anisotropy, *J. Geophys. Res.*, **101**, 28085 – 28103.

Yu, W., Wen, L., & Niu, F., 2005. Seismic velocity structure in the Earth's outer core, *J. Geophys. Res.*, **110**.

Zieglera, K., Younga, E. D., Schaubleb, E. A., & Wassona, J. T., 2010. Metal – silicate silicon isotope fractionation in enstatite meteorites and constraints on Earth's core formation, *Earth Planet. Sci. Lett.*, **295**, 587 – 496.

Zou, Z., Koper, K. D., & Cormier, V. F., 2008. The structure of the base of the outer core inferred from seismic waves diffracted around the inner core, *J. Geophys. Res.*, **113**.

Table 1. Principal energy sources affecting core growth. Parameters are listed in Table 2.

Contribution	Expression
Secular Cooling	$\mathrm{Q_S} \approx \frac{4\pi}{3} b^3 C_p \rho \frac{\partial T_a}{\partial t} = \frac{8\pi}{3} \rho C_p b \Theta_0 c \frac{\mathrm{d}c}{\mathrm{d}t}$
Latent Heat	$\mathrm{Q_L} \approx 4\pi c^2 \rho L \frac{\mathrm{d}c}{\mathrm{d}t}$
Gravitational Energy	$\mathrm{Q_G} \approx \frac{8\pi^2}{5} G\rho\Delta\rho b^2 c^2 \frac{\mathrm{d}c}{\mathrm{d}t}$

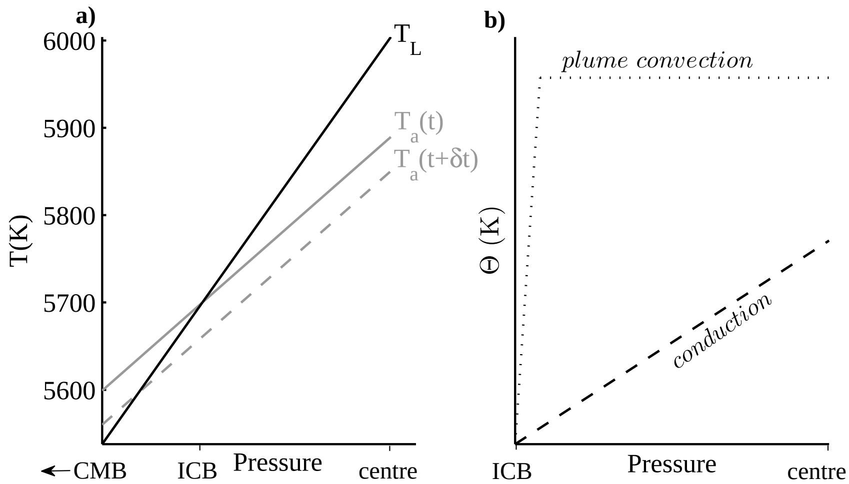

Figure 1. a) Temperature profile in the present-day inner core. The liquidus (T_L) and adiabatic (T_a) profiles intersect at the inner core boundary (ICB). As the core loses heat, the adiabatic profile decreases ($T_a(t+\delta t)$) and so the liquidus and adiabat intersect at a lower pressure, hence the inner core grows. b) Schematic of potential temperature, Θ, in the inner core for superadiabatic conduction (dashed line) and vigorous plume convection (dotted line), where a thin boundary layer develops below the ICB.

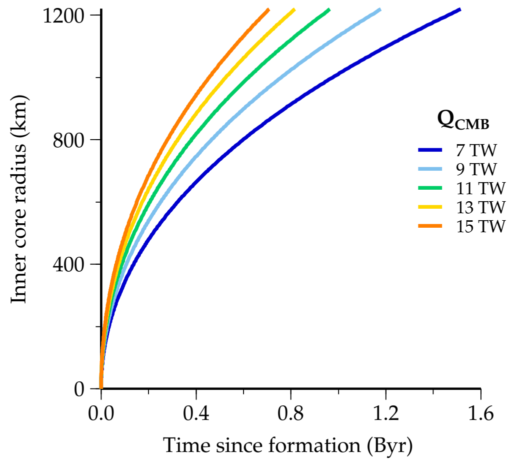

Figure 2. Growth of the inner core for an estimated range of $\mathrm{Q_{CMB}}$ values (Lay et al. 2008), using parameter values in Table 2. For a current inner core radius of 1221.5 km, the age of the inner core ranges from 0.7 to 1.5 Byr.

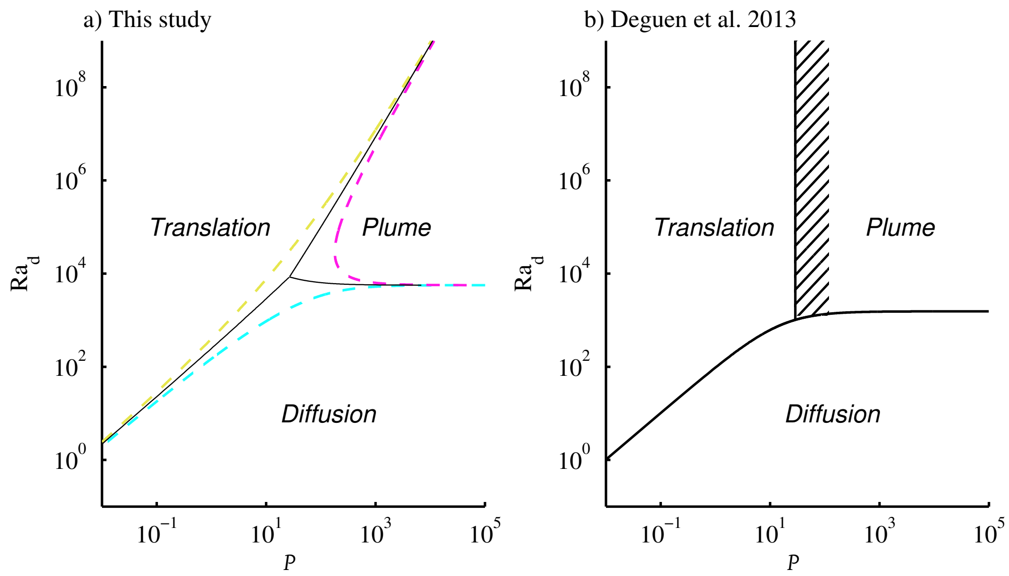

Figure 3. Regime diagrams plotted for the Rayleigh number, $\mathrm{Ra_d}$, versus the parameter, $\mathcal{P}$, defined by Deguen et al. (2013). a) Regime diagram for this study calculated using the quasi-steady state approximation detailed in Appendix C. Dashed lines show when one mode of heat flux is equal to the sum of other two modes - i.e. dashed yellow line indicates when flux from translation is equal to the sum of the plume and diffusive fluxes. Solid lines indicate when one mode is greater than the other two (Table 3) b) Regime diagram from Deguen et al. (2013) calculated for the full set of governing equations (see Figure 13a, Deguen et al. (2013)).

Table 2. Inner core parameter values.

Parameter		Units	Value	Source
CMB heat flow	Q_{CMB}	W	11×10^{12}	Gomi et al. (2013); Hernlund et al. (2005)
ICB temperature	T_L	K	5700	Alfè et al. (2002)
Density	ρ	kg m^{-3}	12900	Dziewonski & Anderson (1981)
Specific heat	C_p	J kg^{-1} K^{-1}	840	Nimmo (2009)
Latent heat	L	kJ kg^{-1}	660	Labrosse (2003)
Thermal expansivity	α	K^{-1}	1.1×10^{-5}	Vocadlo (2007)
Grüneisen parameter	γ		1.4	Vocadlo et al. (2003)
Isothermal bulk modulus	K_T	Pa	1.2×10^{12}	Vocadlo et al. (2003)
Liquidus gradient	$\frac{\partial T_L}{\partial P}$	K Pa^{-1}	1×10^{-8}	$2(\gamma - \frac{1}{3})\frac{T_L}{K_T}$ (Lindemann's law)
Adiabatic gradient	$\frac{\partial T_a}{\partial P}$	K Pa^{-1}	6.3×10^{-9}	$\frac{\alpha T_L}{\rho C_p}$
Thermal conductivity	k	W m^{-1} K^{-1}	36 – 200	Stacey & Davis (2008); de Koker et al. (2012)
Thermal diffusivity	κ	m^2 s^{-1}	4.2×10^{-6}	$\frac{k}{\rho C_p}$
Dynamic viscosity	η	Pa s	10^{18}	Dumberry & Bloxham (2002)
Kinematic viscosity	ν	m^2 s^{-1}	7.8×10^{13}	$\frac{\eta}{\rho}$
Outer core fluid velocity	u	m s^{-1}	10^{-4}	Bloxham & Jackson (1991)
Density jump at ICB	$\Delta\rho$	kg m^{-3}	600	Dziewonski & Anderson (1981)
Present inner core radius	c_0	km	1221.5	Dziewonski & Anderson (1981)
Outer core radius	b	km	3480	Dziewonski & Anderson (1981)
Gravitational constant	G	m^3 kg^{-1} s^{-2}	6.674×10^{-11}	

Table 3. Heat flux ratios for each mode of convection.

Dominant mode	Heat flux
Plume convection	$q_{plume} > q_{trans},\ q_{diff}$
Translation	$q_{trans} > q_{plume},\ q_{diff}$
No convection	$q_{diff} > q_{plume},\ q_{trans}$

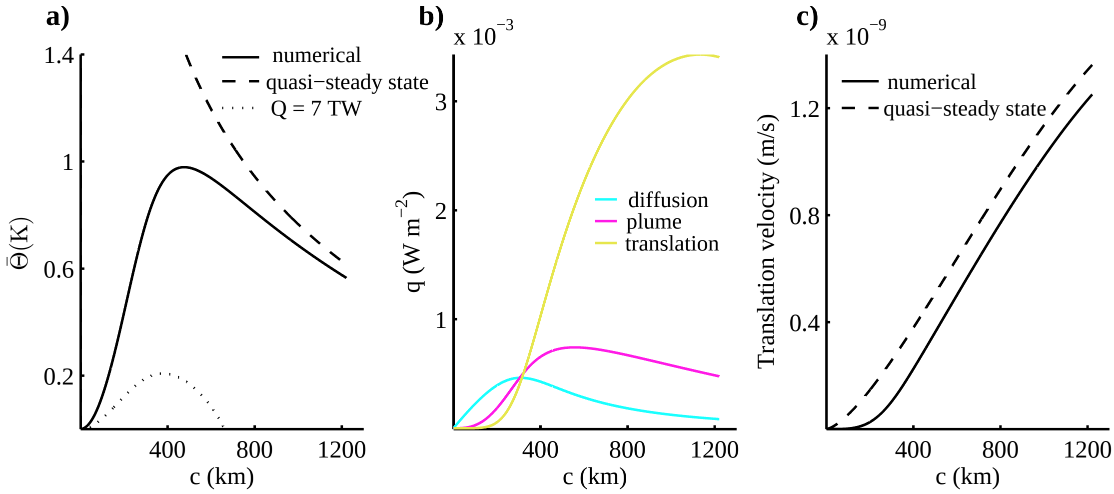

Figure 4. Thermal evolution of the inner core for parameter values in Table 2, with k = 36 W/m/K and Q_{CMB} = 11 TW. a) Mean potential temperature, $\bar{\Theta}$, calculated numerically (solid line), with Q_{CMB} = 7 TW (dotted line) for comparison, and using the quasi-steady state approximation (with Q_{CMB} = 11 TW, dashed line). b) Heat flux lost by diffusion (cyan), plume convection (magenta) and translation (yellow). c) Translation velocity calculated numerically (solid line) and using the quasi-steady state approximation (dashed line).

Table 4. Inner core compositional parameter values. PREM values use the model of Dziewonski & Anderson (1981).

Parameter	Units	Value		Source
Boltzmann's constant k_B	eV/K	8.617×10^{-5}		
		Oxygen	**Sulphur**	
Molar compositional expansion coefficient α_c		0.37	0.39	Gubbins et al. (2013)
Diffusivity in solid D	m^2/s	2×10^{-12}	10^{-12}	Gubbins et al. (2013)
Ab initio linear correction, solid λ_s	eV	–	5.9 ± 0.2	Alfè et al. (2002)
Ab initio linear correction, liquid λ_l	eV	3.25 ± 0.2	6.15 ± 0.04	Alfè et al. (2002)
Difference in solid and liquid				
ab initio constants $\mu_l^0 - \mu_s^0$	eV	-2.6 ± 0.2	-0.25 ± 0.04	Alfè et al. (2002)
Liquid mole fraction (PREM) $\bar{\chi}_l$	mol/mol	0.08 ± 0.025	0.1 ± 0.025	Alfè et al. (2002)
Solid mole fraction (PREM) $\bar{\chi}_s$	mol/mol	0	0.0802	Gubbins et al. (2013)

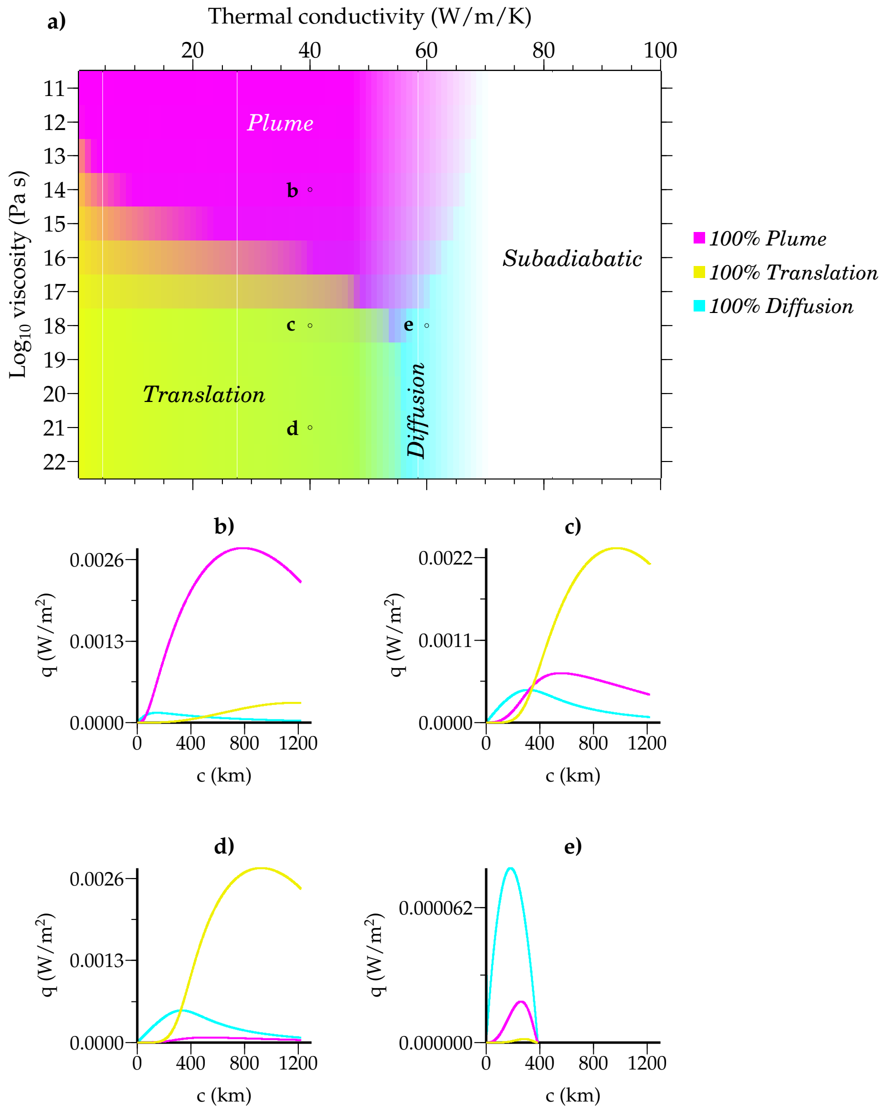

Figure 5. a) Dominant convective mode for a range of estimated inner core viscosity and thermal conductivity values (using Q_{CMB} = 11 TW) , with colours corresponding to the amount of time the inner core has spent in each mode. Profiles for several thermal conductivity and viscosity values are shown for: b) k = 40 W/m/K, $\eta = 10^{14}$ Pa s; c) k = 40 W/m/K, $\eta = 10^{18}$ Pa s; d) k = 40 W/m/K, $\eta = 10^{21}$ Pa s; e) k = 60 W/m/K, $\eta = 10^{18}$ Pa s.

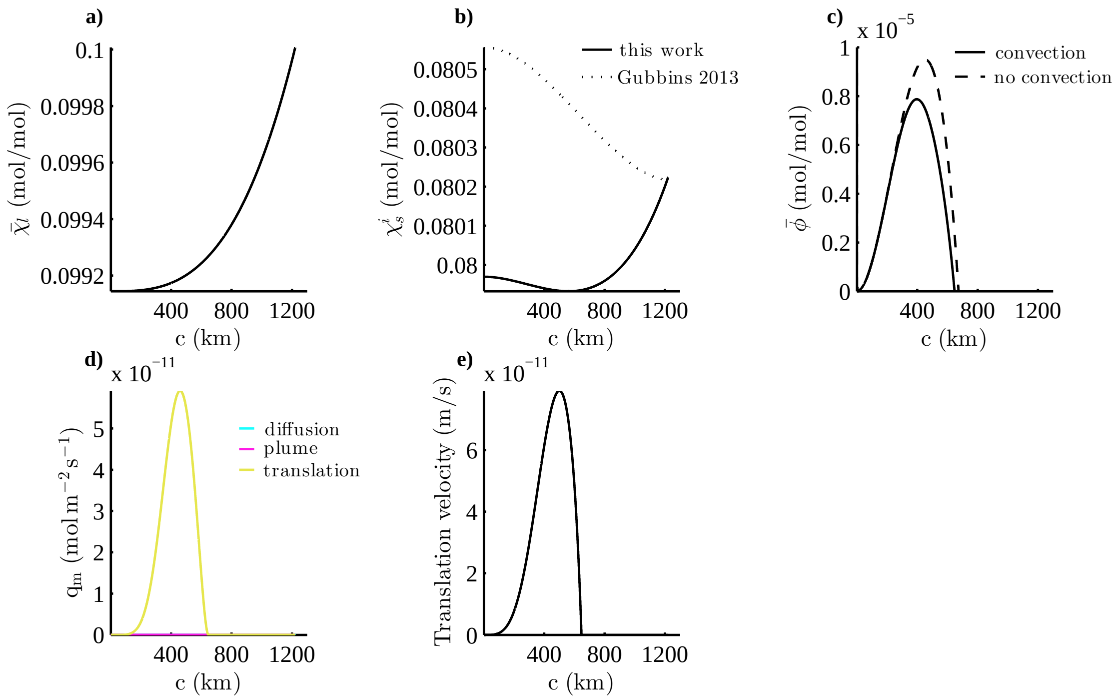

Figure 6. Evolution of sulphur with increasing radius of the inner core with parameter values from Tables 2 and 4. a) Outer core composition, $\bar{\chi}_l$. b) Solid composition at the ICB, χ_s^i, from (58) (solid line) and using the approximations of Gubbins et al. (2013) (dashed line). c) Potential composition in the inner core, $\bar{\phi}$, with (solid line) and without (dashed line) inner core convection. d) Flux from diffusion (cyan), plume convection (magenta) and translation (yellow). e) Translation velocity.

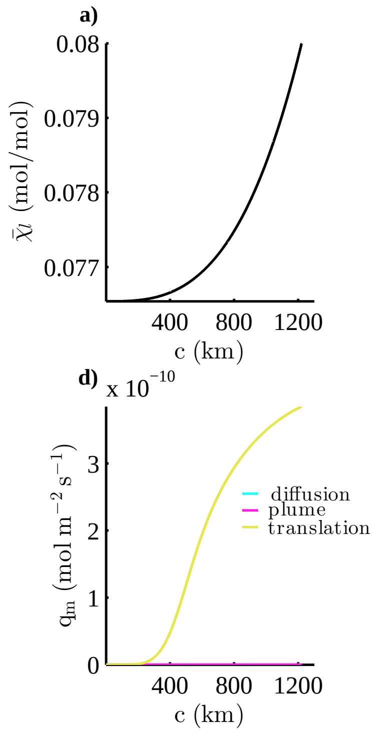

Figure 7. Evolution of oxygen with increasing radius of the inner core with parameter values from Tables 2 and 4. a) Outer core composition, $\bar{\chi}_l$. b) Solid composition at the ICB, χ_s^i, from (58) (solid line) and using the approximations of Gubbins et al. (2013) (dashed line). c) Potential composition in the inner core, $\bar{\phi}$, with (solid line) and without (dashed line) inner core convection. d) Flux from diffusion (cyan), plume convection (magenta) and translation (yellow). e) Translation velocity.

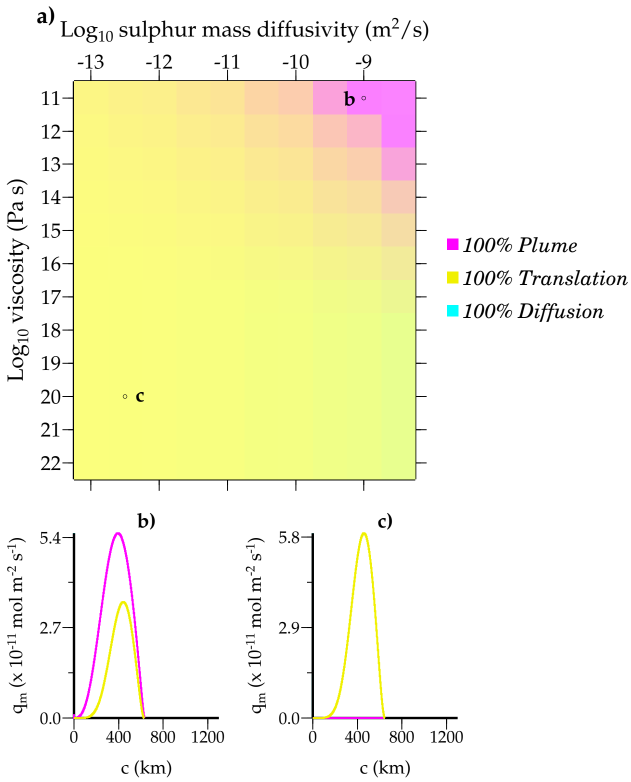

Figure 8. a) Dominant convective mode for a range of estimated inner core viscosity and sulphur solid diffusivity values, with colours corresponding to the amount of time the inner core has spent in each mode. Profiles for several diffusivity and viscosity values are shown for b) D_s = 10^{-9} m^2/s, η = 10^{11} Pa s and c) D_s = 5 $\times$ 10^{-13} m^2/s, η = 10^{20} Pa s.

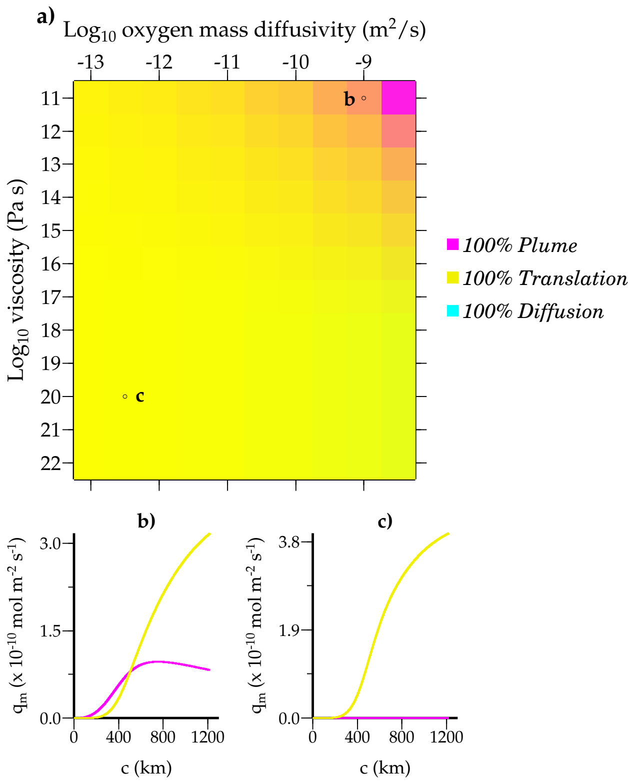

Figure 9. a) Dominant convective mode for a range of estimated inner core viscosity and oxygen solid diffusivity values, with colours corresponding to the amount of time the inner core has spent in each mode. Profiles for several diffusivity and viscosity values are shown for b) $D_o = 10^{-9}$ m^2/s, $\eta = 10^{11}$ Pa s and c) $D_o = 5 \times 10^{-13}$ m^2/s, $\eta = 10^{20}$ Pa s.

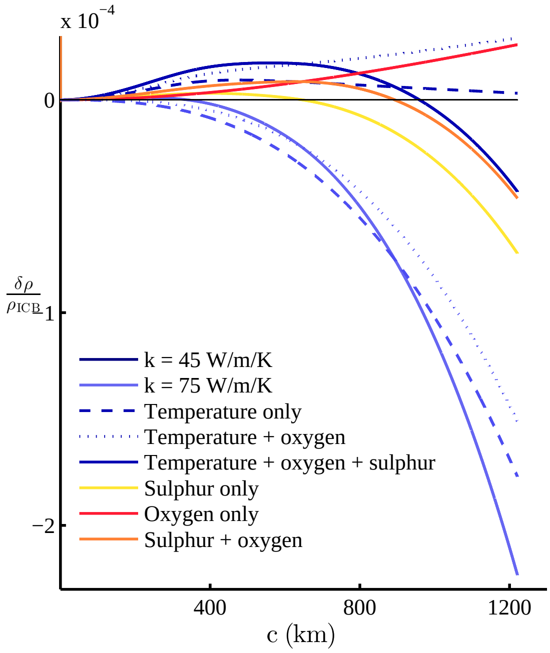

Figure 10. Density anomaly relative to an adiabatic reference state approximated from (72) for two values of inner core conductivity and a combination of thermal and compositional effects.

APPENDIX A: VALIDITY OF THE HEAT FLUX PARAMETRISATION

In this work we have chosen to parametrise the heat flux as a direct sum of terms representing heat flux due to conduction, plume convection and translation. Each of these terms are given by asymptotic expressions which formally only apply when a single mode of heat transport dominates. Consequently, our direct sum heat flux parametrisation will accurately estimate the heat flux in the parameter regimes where a single mode of heat transport dominates, but may be a poor approximation in the transition regions between modes.

Figure A1 shows an example of the potential benefits and shortcomings of our approach. The observed Nusselt number–Rayleigh number relationship for a series of 2D numerical simulations of plume convection by McKenzie et al. (1974) is plotted in red. In these simulations the Nusselt number, Nu, is 1 until the critical Rayleigh number ($\mathrm{Ra_c}$) is reached (the onset of convection), at which point the Nusselt number steadily increases with increasing Rayleigh number as convection becomes more vigorous. At large Rayleigh numbers there is an asymptotic scaling of $\mathrm{Nu} \sim B\mathrm{Ra}^{\frac{1}{3}}$ with $B = 0.23$. The Nusselt number–Rayleigh number relationship given by our direct sum parametrisation of the heat flux is plotted in blue, which yields $\mathrm{Nu} = 1 + B\mathrm{Ra}^{\frac{1}{3}}$. In this case our approximation overestimates the heat flux by up to a factor of 3, with the approximation being poorest near the critical Rayleigh number and best at the extremes of large and small Rayleigh number.

We use the direct sum approximation to determine the dominant mode of heat transport, by assuming that the form of heat transport with the largest contribution to the total heat flux is that which is dominant. In the context of Figure A1, this means that any regime with $\mathrm{Nu} > 2$ is considered plume-convection-dominated, and anything with $\mathrm{Nu} < 2$ is diffusion-dominated. This transition happens at a particular critical Rayleigh number $\mathrm{Ra_c} \sim 100$ shown in blue, slightly less than the true critical Rayleigh number for convection $\mathrm{Ra_c} \sim 657$ shown in red. It is important to note that the transition between conduction and convection is controlled by the correct dimensionless parameter (the Rayleigh number), and only the numerical value of the transition point differs. Thus our direct sum parametrisation is likely to be a good guide to the true behaviour of the system, at the very least in an order-of-magnitude sense.

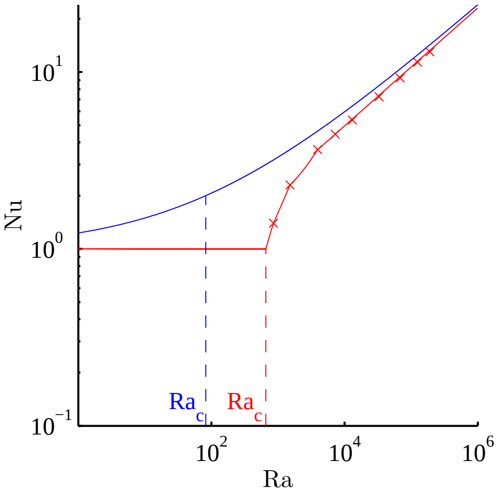

Figure A1. Nusselt number, Nu, versus the Rayleigh number, Ra, for the 2D numerical convection experiment of McKenzie et al. (1974) (red). Nu equals 1, until Ra reaches a critical value ($\mathrm{Ra_c}$), when the system begins to convect and the profile tends to the scaling of $\mathrm{Nu} \sim B\mathrm{Ra}^{\frac{1}{3}}$ for $\mathrm{Ra} \gg \mathrm{Ra_c}$, where B is 0.23 in this case. We approximate the Nusselt number–Rayleigh number scaling to be $\mathrm{Nu} = 1 + B\mathrm{Ra}^{\frac{1}{3}}$ (blue line). Our approximation leads to a slightly different critical Rayleigh number, $\mathrm{Ra_c}$ (blue), and results in an over-estimate of the heat flux in this intermediate area. However our approximation matches the true scaling for high and low Rayleigh numbers.

We also investigate the accuracy of our direct sum parametrisation by looking at the transition from translation to plume dominated convection. The numerical simulations of Deguen et al. (2013) show that this transition is governed by the emergence of secondary flow and smaller scale convection. The secondary flow redistributes the hemispherical density anomalies associated with translation, decreasing the strength of translation until the translation mode disappears.

Figure A2 shows the variation of normalised translation velocity versus the phase change parameter, $\mathcal{P}$, from (52). We define the normalised translation velocity, V_{tr}/V_0,

$$\frac{V_{tr}}{V_0} = \frac{8}{\sqrt{30}}\sqrt{\frac{\mathrm{Ra}}{\mathcal{P}}}\Theta', \tag{A.1}$$

where V_{tr} is the translation rate from (43) and V_0 is the quasi-steady state translation rate from (50). We calculate (A.1) using Θ' obtained assuming the vigorous convection approximation in (C.9) for given values of $\mathrm{Ra_d}$ and $\mathcal{P}$ (Figure A2 is plotted for $\mathrm{Ra_d}/\mathcal{P} = 10^5$). As Figure A2a shows, the rate of translation slows as $\mathcal{P}$ increases, since the plume mode of convection emerges (blue dots). Also plotted is the $\mathcal{O}(\mathcal{P})$ analytical solution of Deguen et al. (2013) (black line), which again shows a decrease in the translation rate with increasing $\mathcal{P}$, but with a much sharper drop off. This is because our parameterised model does not account for secondary flow which is an intermediate regime occurring in the transition between translation and plume convection and this results in an over-estimate of the strength of translation at large $\mathcal{P}$.

Figure A2b shows the average radial heat flux due to translation, divided by the total radial heat flux due to translation and plume convection. This decreases as $\mathcal{P}$ increases, since translation becomes less vigorous. We define the transition from translation to plume dominated convection to be when the heat flux from translation is greater than a combination of other modes, i.e. when $q_{trans}/(q_{trans}+q_{plume}) = 0.5$. This transition occurs when $\mathcal{P} \simeq 10^4$ for $\mathrm{Ra_d}/\mathcal{P} = 10^5$ (blue dashed line, Figure A2b), although the critical value of $\mathcal{P}$ changes with $\mathrm{Ra_d}/\mathcal{P}$. In contrast Deguen et al. (2013) find the transition from translation to plume modes to be independent of $\mathrm{Ra_d}$ and so occurs at approximately $\mathcal{P} \simeq 29$. Deguen et al. (2013)'s value is when the mean degree of kinetic energy becomes greater than 1, i.e. when smaller scale convective modes first appear. This definition of the transition from translation to plume modes is different from ours, which is based on heat flux. We define the transition to be the point at which plume convection is dominant and obeys the asymptotic scaling relationship $\mathrm{Nu} \sim \mathrm{Ra}^{\frac{1}{3}}$; Deguen et al. (2013) define the transition is terms of the shape of internal flow and is when the first small scale modes emerge.

A more accurate parametrisation of the heat flux that more closely resembles the heat flux relationships seen in numerical solutions to the full set of governing equations (such as those by Deguen et al. (2013)) would be favourable. However, constructing such a parametrisation is non-trivial and is a topic for future work. Nevertheless, we expect that the simple direct sum parametrisation we use here has captured the leading-order-behaviour of the system, which is most important given the large uncertainties in parameter values.

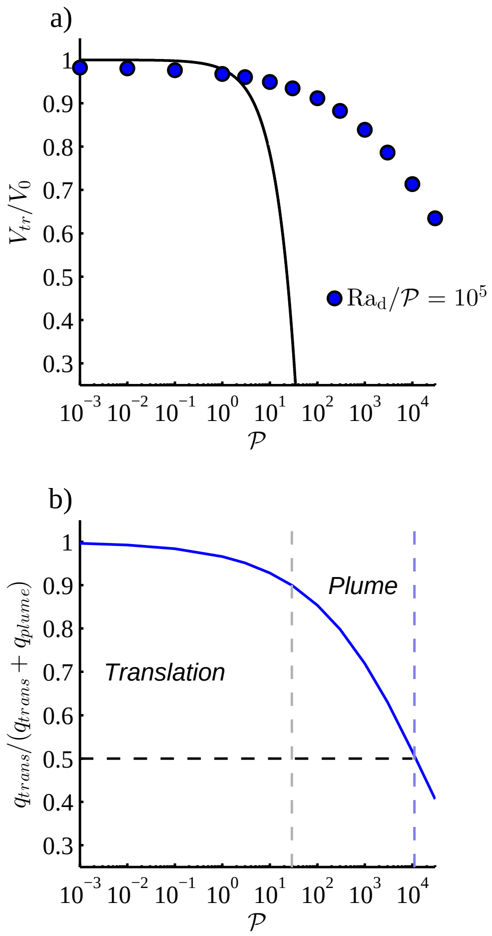

Figure A2. a) Normalised translation velocity given by (A.1) as a function of the phase change parameter, $\mathcal{P}$, for our parameterised model (blue dots) and for the $\mathcal{O}(\mathcal{P})$ analytical solution of Deguen et al. (2013) (black line), calculated for $\mathrm{Ra_d}/\mathcal{P} = 10^5$. b) Average radial heat flux due to translation, q_{trans}, divided by the total radial heat flux due to plume convection and translation, $q_{plume} + q_{trans}$ (blue line). The transition from translation to plume dominated convection occurs in our model when $\mathcal{P} \simeq 10^4$ (blue dashed line), where as the numerical simulations of Deguen et al. (2013) find a transition when $\mathcal{P} \simeq 29$ (grey dashed line).

APPENDIX B: NON-DIMENSIONAL GROWTH AND THERMAL MODEL

We solve our model as a system of non-dimensional equations as outlined below, using the thermal scalings given in Table A1. We non-dimensionalise (2) to express the inner core growth model as

$$\frac{1}{\eta}\frac{\mathrm{d}t'}{\mathrm{d}\eta} = \mathcal{M}[2 + 3\eta(\mathcal{G} + \mathcal{L})]. \tag{B.1}$$

Table A1. Non-dimensional scalings.

Non-dimensional parameters	
$\eta = \frac{c}{b}$	
$\bar{\Theta}' = \frac{\bar{\Theta}}{\Theta_0}$	
Thermal	**Compositional**
$t' = \frac{t\kappa}{b^2}$	$t' = \frac{tD}{b^2}$
$q' = \frac{qb}{k\Theta_0}$	$q' = \frac{qb}{D}$
$\mathcal{M} = \frac{\mathcal{R}}{\kappa}$	$\mathcal{M}_c = \frac{\mathcal{R}}{D}$

We non-dimensionalise the governing equation (45) and combine with the growth model (B.1), such that it becomes

$$\frac{d\bar{\Theta}'}{d\eta} = \mathcal{S}' - \frac{3\bar{\Theta}'}{\eta} - 3q'\mathcal{M}[2 + 3\eta(\mathcal{G} + \mathcal{L})] \tag{B.2}$$

where

$$\mathcal{S}' = 2\left(\eta - 3\frac{\frac{\partial T_a}{\partial P}}{\frac{\partial T_L}{\partial P} - \frac{\partial T_a}{\partial P}}\frac{\mathrm{d}t'}{\mathrm{d}\eta}\right). \tag{B.3}$$

$\tilde{q}'$ is the heat flux due to diffusion, plume convection and translation

$$\tilde{q}' = q'_{diff} + q'_{plume} + q'_{trans} \tag{B.4}$$

where

$$q'_{diff} = \frac{5\bar{\Theta}'}{\eta}, \tag{B.5}$$

$$q'_{plume} = B\,\mathrm{Ra}_0{}^{1/3}\eta^{1/3}\bar{\Theta}'^{4/3}, \tag{B.6}$$

$$q'_{trans} = \frac{32}{135}\,\mathrm{H}_0\,\bar{\Theta}'^{\,2}\,\eta^2, \tag{B.7}$$

and

$$\mathrm{Ra}_0 = \frac{g'\alpha b^4\Theta_0}{\nu\kappa}\,,\ \mathrm{H}_0 = \frac{uC_p\rho_l\alpha b\Theta_0^2}{L\Delta\rho\kappa}. \tag{B.8}$$

The translation velocity, (42), becomes

$$V' = \frac{8}{15}\mathrm{H}_0\eta^2\bar{\Theta}'. \tag{B.9}$$

APPENDIX C: DOMINANT REGIMES IN THE QUASI-STEADY STATE APPROXIMATION

Following from section 3.3.1, assuming that convection in the inner core is vigorous, we write a quasi-steady state approximation as

$$q \sim \frac{\rho C_p c \mathcal{S}}{3}. \tag{C.1}$$

We non-dimensionalise our model, using the scalings defined below, in order to compare it to the model of Deguen et al. (2013). First, we define q_r as

$$q_r = \rho C_p c \mathcal{S} = \frac{k\Theta_r}{c} \tag{C.2}$$

and so Θ_r is defined by

$$\Theta_r = \frac{\rho C_p c^2 \mathcal{S}}{k}. \tag{C.3}$$

We use q_r and Θ_r to non-dimensionalise the heat flux, q, and the mean potential temperature, $\bar{\Theta}$, respectively

$$\tilde{q} = \frac{q}{q_r} = \frac{q}{\rho C_p c \mathcal{S}} = \frac{\rho C_p c \mathcal{S}}{3\rho C_p c \mathcal{S}} = \frac{1}{3} \tag{C.4}$$

and

$$\Theta' = \frac{\bar{\Theta}}{\Theta_r}. \tag{C.5}$$

We now non-dimensionalise each heat flux term independently using the scaling q_r. The expression for diffusion flux becomes

$$\tilde{q}_{diff} = \frac{q_{diff}}{q_r} = 5\Theta'. \tag{C.6}$$

Plume flux is expressed

$$\tilde{q}_{plume} = \frac{q_{plume}}{q_r} = B6^{\frac{1}{3}} \mathrm{Ra_d}^{\frac{1}{3}} \Theta'^{\frac{4}{3}}, \tag{C.7}$$

where $\mathrm{Ra_d}$ is the Rayleigh number defined in (51). Lastly the heat flux from translation is expressed,

$$\tilde{q}_{trans} = \frac{q_{trans}}{q_r} = \frac{32}{45}\left(\frac{\mathrm{Ra_d}}{\mathcal{P}}\right)\Theta'^2 \tag{C.8}$$

where $\mathcal{P}$ is the dimensionless 'phase change' parameter from Deguen et al. (2013), defined in (52). From C.4, we know that

$$\tilde{q} = \tilde{q}_{diff} + \tilde{q}_{plume} + \tilde{q}_{trans} = \frac{1}{3}. \tag{C.9}$$

The boundaries between the 3 regimes are defined as

$$\tilde{q}_{diff} = \tilde{q}_{plume}, \tag{C.10}$$

$$\tilde{q}_{diff} = \tilde{q}_{trans} \text{ and} \tag{C.11}$$

$$\tilde{q}_{plume} = \tilde{q}_{trans}. \tag{C.12}$$

In order to highlight the transition areas between regimes, we also calculated the boundaries when one mode is equal to the sum of the remaining 2 modes, i.e.

$$\tilde{q}_{diff} = \tilde{q}_{plume} + \tilde{q}_{trans} = \frac{1}{6} \tag{C.13}$$

$$\tilde{q}_{plume} = \tilde{q}_{diff} + \tilde{q}_{trans} = \frac{1}{6}, \text{ and} \tag{C.14}$$

$$\tilde{q}_{trans} = \tilde{q}_{diff} + \tilde{q}_{plume} = \frac{1}{6}. \tag{C.15}$$

We solve for the regime boundaries numerically to plot the regime diagram, of Ra versus $\mathcal{P}$ in Figure 3. To calculate the regime boundaries (solid lines, Figure 3a) we solve for (C.9) together with one of (C.10), (C.11) or (C.12) depending on the boundary of interest. To calculate the boundaries when one mode becomes dominant (when the mode is equal to the sum of the remaining modes, dashed lines, Figure 3a), we first solve for Θ' using a given value of Ra and either one of (C.6), (C.7) or (C.8) depending on the regime we are interested in. The critical value of $\mathcal{P}$ is then calculated from one of (C.13), (C.14) or (C.15).

APPENDIX D: NON-DIMENSIONAL COMPOSITIONAL MODEL

D1 Compositional convection

As for the thermal model, we non-dimensionalise the governing equation, (63), this time using the compositional scalings in Table A1 and we combine with the growth model in (B.1), such that the governing equation becomes

$$\frac{d\bar{\phi}}{\mathrm{d}\eta} = -\mathcal{S}_c - \frac{3\bar{\phi}}{\eta} - 3q'_m\mathcal{M}_c(2 + 3\eta(\mathcal{G} + \mathcal{L})). \tag{D.1}$$

q'_m is the molar flux due to diffusion, plume convection and translation

$$q'_m = q'_{diff} + q'_{plume} + q'_{trans} \tag{D.2}$$

where

$$q'_{diff} = \frac{5\bar{\phi}}{\eta}, \tag{D.3}$$

$$q'_{plume} = B\mathrm{Ra_c}^{\frac{1}{3}}\bar{\phi}^{\frac{4}{3}}\eta^{\frac{1}{3}}, \tag{D.4}$$

$$q'_{trans} = \frac{32}{135}\mathrm{H_c}\eta^2\bar{\phi}^2 \tag{D.5}$$

and

$$\mathrm{Ra_c} = \frac{g'b^4\alpha_c}{\nu D}, \mathrm{H_c} = \frac{uC_p\rho_l\alpha_c b\Theta_0}{L\Delta\rho D}. \tag{D.6}$$

The non-dimensional translation velocity is

$$V' = \frac{8}{15}\mathrm{H_c}\eta^2\bar{\phi}. \tag{D.7}$$

D2 Solution to compositional convection

We solve the governing compositional convection equations as a system of differential algebraic equations. Firstly we substitute (62) – re-arranged for the average inner core composition, $\bar{\chi}_s$ – into (59) such that the mean liquid composition, $\bar{\chi}_l$, is a function of the mean potential composition, $\bar{\phi}$, i.e.

$$\bar{\chi}_l = \frac{\chi_0 - \eta^3\bar{\chi}_s}{1 - \eta^3} = \frac{\chi_0 - \eta^3(\bar{\phi} + \chi_s^i)}{1 - \eta^3}. \tag{D.8}$$

This expression for $\bar{\chi}_l$ is now substituted into (58) in order to remove the dependence of χ_s^i on $\bar{\chi}_l$

$$\chi_s^i(c) = \frac{k_B T_L(c)}{\lambda_s}\mathcal{W}\left(\frac{\chi_0 - \eta^3(\bar{\phi} + \chi_s^i)\lambda_s}{k_B T_L(c)(1 - \eta^3)}\exp\left(\frac{\lambda_l\frac{\chi_0 - \eta^3(\bar{\phi} + \chi_s^i)}{1 - \eta^3} + \mu_l^0 - \mu_s^0}{k_B T_L(c)}\right)\right). \tag{D.9}$$

Finally we re-write the governing equation (D.1) as

$$\frac{d\bar{\phi}}{\mathrm{d}\eta} + \frac{d\chi_s^i}{\mathrm{d}\eta} = -\frac{3\bar{\phi}}{\eta} - 3q'\mathcal{M}_c(2 + 3\eta(\mathcal{G} + \mathcal{L})) \tag{D.10}$$

in order to solve for $\bar{\phi}$ and χ_s^i by casting (D.9) and (D.10) as a system of differential algebraic equations.